Multi-omics Analysis of CRISPRi-Knockdowns Identifies Mechanisms that Buffer Decreases of Enzymes in E. coli Metabolism

Donati, Stefano; Kuntz, Michelle; Pahl, Vanessa; Farke, Niklas; Beuter, Dominik; Glatter, Timo; Gomes-Filho, José Vicente; Randau, Lennart; Wang, Chun Ying; Link, Hannes

Published in:
Cell Systems

Link to article, DOI:
10.1016/j.cels.2020.10.011

Publication date:
2021

Document Version
Publisher's PDF, also known as Version of record

Cell Systems

Article

Multi-omics Analysis of CRISPRi-Knockdowns Identifies Mechanisms that Buffer Decreases of Enzymes in *E. coli* Metabolism

Graphical Abstract

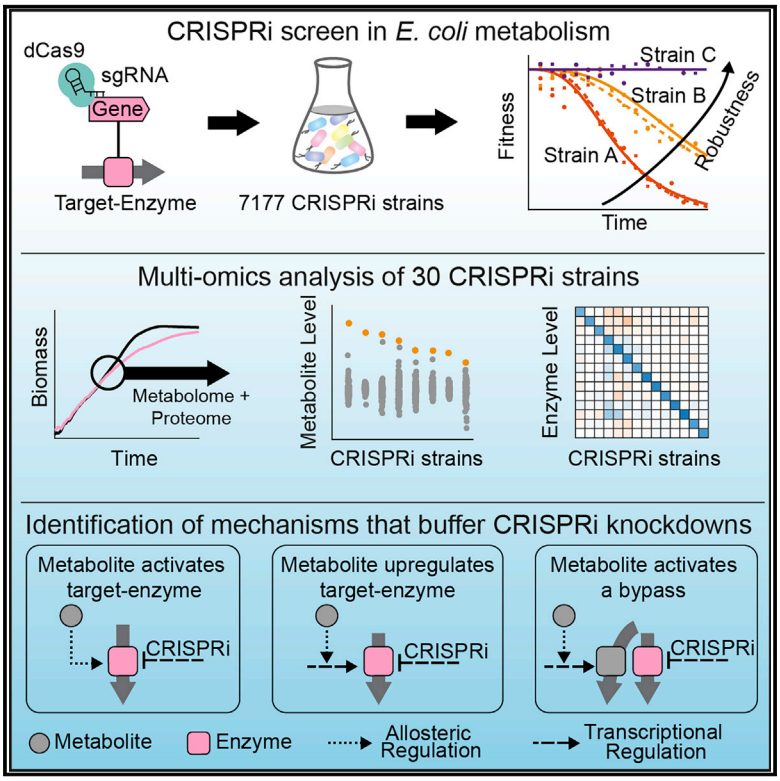

Highlights

- An inducible CRISPRi system identifies rate-limiting enzymes
- *E. coli* metabolism is robust against CRISPRi-knockdowns of enzymes
- CRISPRi enforces specific metabolome and proteome responses
- Regulatory metabolites buffer CRISPRi-knockdowns

Authors

Stefano Donati, Michelle Kuntz, Vanessa Pahl, ..., Lennart Randau, Chun-Ying Wang, Hannes Link

Correspondence

hannes.link@
synmikro.mpi-marburg.mpg.de

In Brief

Donati and Kuntz et al., study the consequences of CRISPR interference in *Escherichia coli* metabolism. Their work suggests that metabolism is robust against knockdowns of enzymes and that regulatory metabolite-protein interactions buffer such perturbations.

Donati et al., 2021, Cell Systems *12*, 56–67
January 20, 2021
https://doi.org/10.1016/j.cels.2020.10.011

CellPress

CellPress
OPEN ACCESS

Cell Systems

Article

Multi-omics Analysis of CRISPRi-Knockdowns Identifies Mechanisms that Buffer Decreases of Enzymes in *E. coli* Metabolism

Stefano Donati,[1,2,3] Michelle Kuntz,[1,2,4] Vanessa Pahl,[1,4] Niklas Farke,[1,4] Dominik Beuter,[1] Timo Glatter,[1] José Vicente Gomes-Filho,[1] Lennart Randau,[1] Chun-Ying Wang,[1,4] and Hannes Link[1,4,5,*]

[1]Max Planck Institute for Terrestrial Microbiology, Marburg, Germany
[2]These authors contributed equally
[3]Present Adress: The Novo Nordisk Foundation Center for Biosustainability, Technical University of Denmark, DK-2800 Kgs. Lyngby, Denmark
[4]Present address: Interfaculty Institute for Microbiology and Infection Medicine Tübingen, University of Tübingen, Auf der Morgenstelle 24, 72076 Tübingen, Germany
[5]Lead Contact
*Correspondence: hannes.link@synmikro.mpi-marburg.mpg.de
https://doi.org/10.1016/j.cels.2020.10.011

SUMMARY

Enzymes maintain metabolism, and their concentration affects cellular fitness: high enzyme levels are costly, and low enzyme levels can limit metabolic flux. Here, we used CRISPR interference (CRISPRi) to study the consequences of decreasing *E. coli* enzymes below wild-type levels. A pooled CRISPRi screen with 7,177 strains demonstrates that metabolism buffers fitness defects for hours after the induction of CRISPRi. We characterized the metabolome and proteome responses in 30 CRISPRi strains and elucidated three gene-specific buffering mechanisms: ornithine buffered the knockdown of carbamoyl phosphate synthetase (CarAB) by increasing CarAB activity, S-adenosylmethionine buffered the knockdown of homocysteine transmethylase (MetE) by de-repressing expression of the methionine pathway, and 6-phosphogluconate buffered the knockdown of 6-phosphogluconate dehydrogenase (Gnd) by activating a bypass. In total, this work demonstrates that CRISPRi screens can reveal global sources of metabolic robustness and identify local regulatory mechanisms that buffer decreases of specific enzymes. A record of this paper's transparent peer review process is included in the Supplemental Information.

INTRODUCTION

Enzymes catalyze biochemical reactions that maintain metabolism and cell growth. Correspondingly, expression levels of enzymes influence cellular metabolism and fitness. Growth of *E. coli*, for instance, is affected by the abundance of single enzymes (Dekel and Alon, 2005; Li et al., 2014), as well as by the total mass of catabolic enzymes (You et al., 2013). However, it is not clear to what extent the expression of every single enzyme in a cell influences metabolism and fitness.

The consequences of perturbing enzyme levels were investigated with knockout libraries of yeast and *E. coli* (Baba et al., 2006; Giaever et al., 2002). Studies with these libraries showed that the absence of a single enzyme has very precise and specific effects on metabolism (Fuhrer et al., 2017; Mülleder et al., 2016) and transcription (Kemmeren et al., 2014). However, knockouts are extreme cases and they are not feasible for key metabolic enzymes, which are essential for growth on single carbon sources such as glucose. Moreover, knockouts are static and, therefore, they may reflect metabolic states that have already adapted at the level of gene expression (Hosseini and Wagner, 2018; Ishii et al., 2007) or by mutations (McCloskey et al., 2018a). Thus, it is difficult to learn about acute responses to perturbations of enzyme levels using gene deletions.

To understand the consequences of enzyme-level perturbations around wild-type levels, a series of studies measured enzyme expression in different environmental conditions (Buescher et al., 2012; Gerosa et al., 2015; Hackett et al., 2016). These studies showed that most enzymes have different expression levels in different conditions and that the average enzyme mass of *E. coli* cells changes more than 2-fold across conditions (Schmidt et al., 2016). However, expression changes across conditions were mainly driven by global growth-dependent regulation (Erickson et al., 2017), and delineating local regulation from these data has proven difficult (Gerosa et al., 2013; Keren et al., 2013). An approach to achieve more specific and localized changes of enzyme levels is to delete regulatory proteins that control enzyme expression. For example, deleting protein kinases in yeast caused widespread and specific changes of enzyme levels (Zelezniak et al., 2018), and deletion of

transcription factors in *E. coli* amino acid biosynthesis led to increases of only the enzymes that belong to the respective regulon (Sander et al., 2019). However, because deletion of regulators affects the expression of many enzymes simultaneously, it is still difficult to decipher which enzyme was responsible for certain metabolic phenotypes.

Thus, it remains an open question as to how cellular metabolism responds to moderate changes of a single enzyme. Such changes can occur in nature due to expression noise (Metzger et al., 2015; Newman et al., 2006) or mutations of genes that encode enzymes (Kacser and Burns, 1981). Control theory suggests that moderate changes of an enzyme have only small and local effects on metabolism, which means that local changes should not propagate globally (Levine and Hwa, 2007; Mazat et al., 1996). This robustness of metabolism is somewhat expected, but mostly theoretical studies examined the mechanisms that enable metabolic robustness (Chandra et al., 2011; Grimbs et al., 2007). The few studies that measured robustness against changes of enzyme abundance focused on specific pathways (Fendt et al., 2010; Tanner et al., 2018), but robustness was not measured at a metabolism-wide level.

Recent developments of targeted genome modification methods have advanced our ability to perturb the expression of single genes with high precision and high throughput. For example, synthetic promoter libraries in yeast mapped the precise relationship between the expression level of genes and cellular fitness (Keren et al., 2016). Many of the 80 target genes in this study encoded key metabolic enzymes and their expression levels had little effect on the fitness of yeast. Another method to modulate gene expression is CRISPR interference (CRISPRi), which represses transcription of a target gene with a complex of deactivated Cas9 (dCas9) and a single guide RNA (sgRNA) (Qi et al., 2013). As CRISPRi is inducible, it permits time-resolved studies (Camsund et al., 2020; Rishi et al., 2020) and functional analyses of genes that are essential and, therefore, not viable in knockout libraries (Peters et al., 2016; Rishi et al., 2020; Rousset et al., 2018). Many CRISPRi screens measured simple phenotypes, such as fitness and growth, but to our knowledge, there is no comprehensive study that combined CRISPRi perturbations in metabolism with multi-omics analysis.

Here, we combined a metabolism-wide CRISPRi screen with multi-omics analysis of 30 CRISPRi strains to investigate how *E. coli* metabolism responds to decreases of enzyme levels. First, we measured the competitive fitness of 7,177 strains in a metabolism-wide CRISPRi library. An inducible CRISPRi system enabled us to measure the time delay between inducer addition and appearance of fitness defects. Only 7 CRISPRi strains responded within the first 4 h after induction of CRISPRi, while fitness defects of most strains appeared with a considerable time delay (in average 7.8 h). This provided the first evidence that *E. coli* metabolism is robust against decreasing enzymes below wild-type levels. The metabolome and proteome of 30 CRISPRi strains showed that changes in the metabolic network were local and specific. For example, target enzymes were always among the most downregulated proteins (on average 5-fold). At the metabolome level, we observed strong concentration changes of substrate metabolites and allosteric effectors. We show, for 3 CRISPRi strains, that these changes contributed to buffering the knockdown: (1) increases of ornithine buffered the CarAB knockdown by allosterically activating the enzyme, (2) S-adenosylmethionine triggered a compensatory upregulation of the methionine pathway in the MetE knockdown, and (3) 6-phosphogluconate was responsible for activation of the Entner-Doudoroff (ED) pathway in the Gnd knockdown. Overall, our results highlight the central role of regulatory metabolites in maintaining robustness against ever-changing concentrations of enzymes in a cell, which occur in nature due to stochastic effects such as expression noise, cell division, or fluctuating environments.

RESULTS

An Inducible CRISPRi System Identifies Rate-Limiting Enzymes

For dynamic knockdowns of enzymes, we used a CRISPRi system that consisted of an aTc-inducible dCas9 on the chromosome (Lawson et al., 2017), and a constitutively expressed sgRNA on a plasmid (Qi et al., 2013) (Figure 1A). To evaluate the dynamics of gene interference with this CRISPRi system, we targeted a YPet reporter protein inserted in the *E. coli* genome (Lawson et al., 2017). These experiments showed an exponential decrease of the YPet content per cell, indicating a constant dilution of the YPet protein by growth (Figure 1B). The 1-h delay between inducer addition and decrease of YPet may be occurring due to the time of dCas9 expression and its target search (Jones et al., 2017). Moreover, YPet expression was only repressed in the presence of the dCas9 inducer aTc, showing tight control of the CRISPRi system (Figure 1B). Thus, CRISPRi allowed us to dynamically decrease the abundance of proteins starting from unrepressed (wild-type) levels.

To further test the dynamics of the CRISPRi system, we targeted genes encoding enzymes in pyrimidine nucleotide biosynthesis. All pyrimidine enzymes are essential for the growth of *E. coli* on glucose minimal medium. Therefore, knockdowns of pyrimidine genes should cause a growth defect when enzyme levels reach a critical threshold. At this threshold, the target enzyme limits biosynthesis of uridine monophosphate (UMP) and, eventually, affects growth (Figure 1C). Expression of dCas9 was either induced by supplementing aTc at the start of the cultivation (induced cultures), or cells were grown without an inducer (uninduced cultures). A control strain without target grew similar in induced and uninduced cultures, which means that dCas9 expression alone causes no growth burden (Figure 1D). Uninduced cultures of all pyrimidine knockdowns grew similar to the control, confirming that the CRISPRi system is tight. Induced cultures, in contrast, displayed a wide range of growth phenotypes: knockdown of the first two enzymes of the pathway (PyrB and PyrC) hardly affected growth, while the PyrE knockdown caused a strong growth defect. Knockdown of PyrF and PyrD impaired growth as well, but the effect appeared relatively late after induction of CRISPRi (around 5 h).

In conclusion, CRISPRi allowed us to induce dynamic decreases in protein-levels (Figure 1B). The 5-h delay between inducer addition and appearance of growth defects in the PyrF and PyrD knockdowns, suggests that the target protein is diluted by growth until it reaches a critical level. In contrast, the early growth defect in the PyrE strain indicates that this enzyme is already expressed at a critical level in the wild type. This is

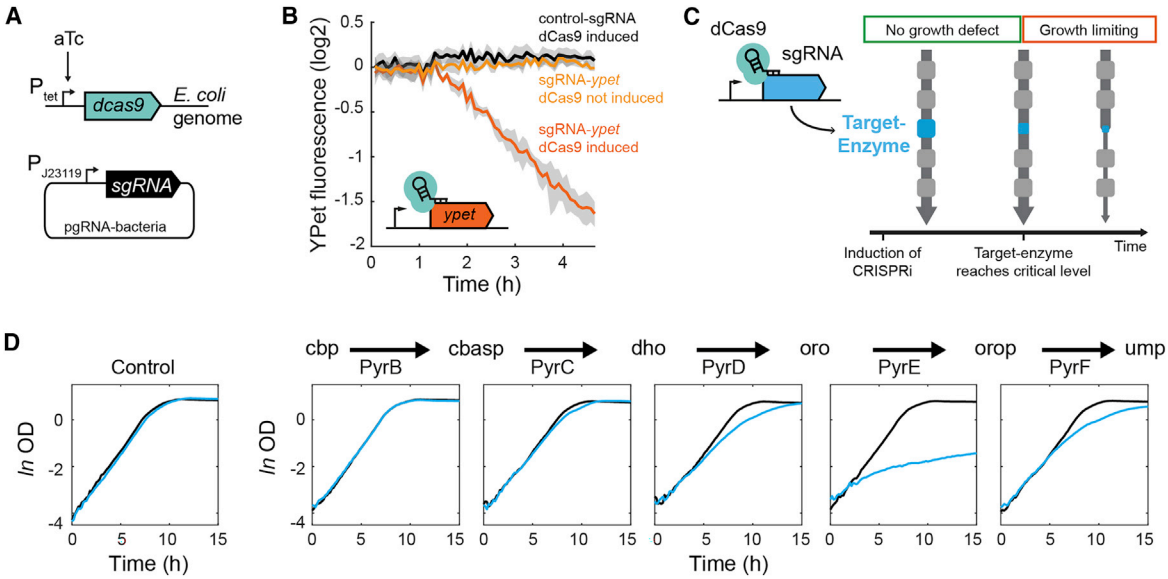

Figure 1. Dynamic Knockdowns of Enzymes with CRISPR Interference

(A) The CRISPR interference system consisted of an *E. coli* strain (YYdCas9) that has dCas9 integrated into the genome (Lawson et al., 2017), and a sgRNA on a plasmid (Qi et al., 2013). dCas9 is under control of an aTc-inducible Ptet promoter. The sgRNA is under control of a constitutive promoter.

(B) Dynamic knockdown of YPet, which is integrated into the genome of the YYdCas9 strain. YPet fluorescence is shown for cells that express either a control sgRNA (black) or a sgRNA that targets YPet (orange). YPet fluorescence per optical density (OD) is normalized to an uninduced culture with the control sgRNA. The YPet knockdown was induced at time = 0 h by supplementing 200 nM of aTc. Data are represented as mean, and the gray areas are ±SD (n = 3).

(C) Knockdown of an enzyme impairs growth when its concentration reaches a critical level. The target enzyme is the enzyme, which is encoded by the gene that is repressed with CRISPRi.

(D) Growth of cells expressing the control sgRNA, or sgRNAs targeting genes that encode enzymes in pyrimidine nucleotide biosynthesis. Expression of dCas9 was induced by supplementing 200 nM of aTc (blue) or dCas9 was not induced (black). Cells grew on minimal glucose medium in microtiter plates. Means of n = 3 cultures are shown.

consistent with previous reports about the suboptimal expression of PyrE in K12-derived *E. coli*, due to a frameshift mutation upstream of the *pyrE* gene (Jensen, 1993). The comparably weaker growth defects of the other pyrimidine knockdowns indicated that these enzymes do not operate at a critical level. However, an alternative explanation is that the sgRNAs for these targets are weaker or not functional. Therefore, we next targeted genes with several sgRNAs and designed sgRNAs for all metabolism-related genes in *E. coli*.

E. coli Metabolism Is Robust against CRISPRi-Knockdowns of Enzymes

The latest genome-scale model of *E. coli* metabolism, *i*ML1515, includes 1,515 genes (Monk et al., 2017), and we constructed sgRNAs that target these genes using array-synthesized oligonucleotides (Figure 2A). Per gene, we designed 4 to 6 sgRNAs that target different loci on the coding strand. The resulting sgRNAs were cloned in a pooled approach and, subsequently, transformed into *E. coli* that carried dCas9 on the genome (Figure 1A). Sequencing of the CRISPRi library showed that 7,177 unique sgRNAs were present in the library and they targeted 1,513 of the 1,515 genes in the *i*ML1515 model (Figure S1; Table S1). We cultured the library for 13 h on glucose minimal medium without induction of dCas9, which hardly changed the composition of the library: the fold change of single CRISPRi strains after 13 h was normally distributed around 1, and only 47 out 7,177 strains (0.6%) showed a fold change >2 (Figure S1). The stable composition of the uninduced library confirms again tight control of the CRISPRi system. Subsequently, we induced dCas9 expression and followed the library composition by next-generation sequencing for 14 h in intervals of 1 h (Figure 2A). Every 2 h, the cultures were back diluted into fresh medium, to avoid limitations of oxygen and nutrients. To assess reproducibility, we used two independent cultivations. Fitness scores of single CRISPRi strains were quantified as fold change of sgRNA counts, which were reproducible between the two independent cultivations (Figure S2).

To explore dynamic patterns of fitness scores of the 7,177 CRISPRi strains in the library, we performed k-means clustering with their individual time profiles (Figure 2B). The fitness scores of 44% of the CRISPRi strains were constant for 14 h (cluster A). Another 32% of the strains in cluster B showed a slight increase in fitness scores. This cluster included a control strain that expressed a sgRNA with no target (orange line in cluster B, Figure 2B). This shows that increasing fitness scores are due to a relative enrichment of strains that have wild-type-like growth. However, some strains had higher fitness scores than the control strain suggesting that these knockdowns confer a competitive advantage over the wild type. Knockdowns of 18 genes resulted in fitness scores >1.5 after 14 h (with at least two sgRNAs, Table S2), thus indicating that expression of these genes is not optimal on glucose minimal medium. Two of the suboptimally expressed genes encoded enzymes that produce important secondary messengers in *E. coli*: cyclic-AMP (*cyaA*) and ppGpp (*relA*). This

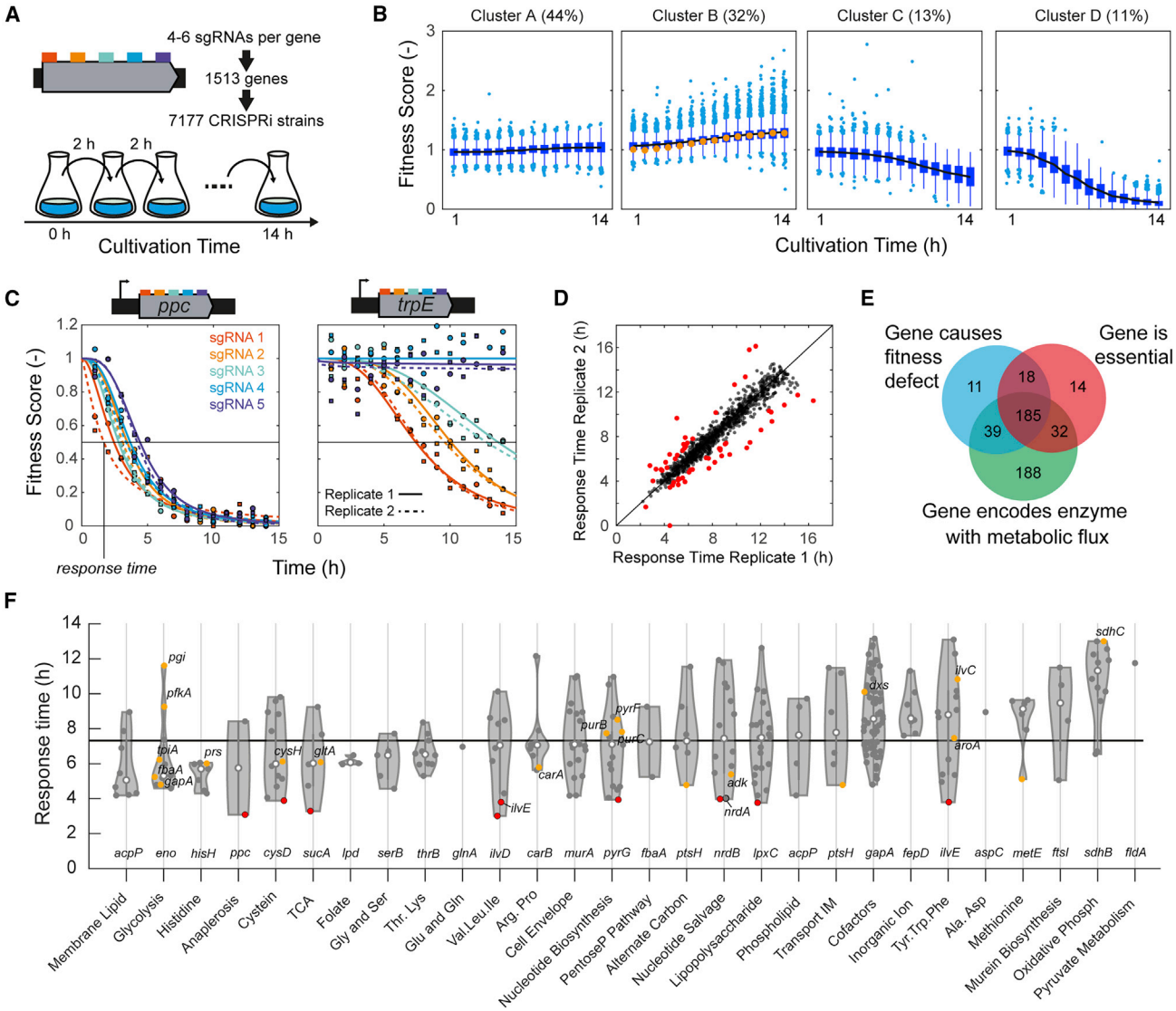

Figure 2. Dynamic Knockdowns of 1,513 Genes in the Metabolic Network of *E. coli*

(A) A CRISPRi library targeting 1,513 genes in the latest genome-scale reconstruction of *E. coli* metabolism (*i*ML1515). Each gene was targeted with 4–6 sgRNAs, which are equally distributed on the coding strand. sgRNAs were cloned in a pooled approach on plasmid pgRNA-bacteria and YYdCas9 was transformed with the resulting plasmid library (see also Figure 1A). The library was induced with 200 nM aTc at time = 0 h, and cultured for 14 h in shaking flasks. The culture was back-diluted every 2 h into fresh medium. Samples for next generation sequencing were collected every hour. See also Table S1.

(B) K-means clustering of fold-changes of 7,177 sgRNAs. Time-course data were clustered into k = 4 clusters. Box plots represent the distribution of sgRNAs in each cluster per time point. Orange dots in cluster B indicate a control strain that expresses a sgRNA with no target. See also Table S2.

(C) Examples of fitness-score dynamics of CRISPRi strains (*ppc* with low variability between 5 sgRNAs and *trpE* with high variability between 5 sgRNAs). Sigmoidal curves were fitted to the time course of each sgRNA. The response time was defined as the time point when the fold-change of a sgRNA was 0.5. Different colors are different sgRNAs. Full and dashed lines are fits to experiment 1 (squares) and experiment 2 (circles).

(D) Response times in experiment 1 and experiment 2. Shown are 1,182 sgRNA that had response times below 14 h (average of experiment 1 and experiment 2). 57 sgRNAs that had more than 20% error are shown in red. See also Table S3.

(E) Venn diagram showing the overlap between 253 "metabolic bottleneck genes" (blue), genes that are essential on glucose minimal medium (red), and genes that encode enzymes with metabolic flux (green).

(F) Response times of all 253 "metabolic bottleneck genes". See also Table S4. Shown is the average response time of the two strongest sgRNAs of each gene. Genes are grouped into metabolic categories according to the definition in *i*ML1515. The name of the most sensitive target is shown for each category. Red dots are genes with response times below 4 h. Orange dots are the 30 targets in Figure 3. See also Figures S1–S4.

observation is consistent with a previous study that showed sub-optimal regulation by cyclic-AMP and ppGpp in *E. coli* (Towbin et al., 2017). We confirmed the fitness advantage of the *relA* strain in microtiter plate cultivations (Figure S3).

The remaining 24% of sgRNAs in cluster C and D caused mild and strong fitness defects, respectively. The sigmoidal dynamics of fitness scores in cluster D suggest that the CRISPRi strains in this cluster drop out from the library, presumably because the

knockdown created a metabolic bottleneck. To identify at which time point the knockdowns created a metabolic bottleneck, we estimated a "response time" for each CRISPRi strain by fitting a sigmoidal function to the time course of the fitness score (Figure 2C; Table S3). The response time was defined as the time point when the knockdown caused a 50% reduction of fitness, and response times were reproducible between the two experiments (Figure 2D). In total, 253 genes were targeted by at least two sgRNAs that caused response times below 14 h, and we refer to these 253 targets as metabolic-bottleneck genes (Table S4). Most metabolic-bottleneck genes had similar response times for the 4–6 sgRNAs: 70% had responses times that varied less than ±20% between different sgRNAs (Figure S4). The different sgRNAs bind at different positions of the target genes, and therefore they should have different repression efficiencies (Qi et al., 2013). Yet, the position hardly affected response times (Figure S4). This result indicates that repression efficiencies have smaller effects on response times than target-specific factors.

The majority of the metabolic-bottleneck genes (203 out of 253; 80%) are essential for growth on glucose medium (Figure 2E). According to simulations with the *i*ML1515 model, 224 of the 253 metabolic-bottleneck genes (88%) encode enzymes that carry metabolic flux with glucose as a sole carbon source. Only 11 genes (4%) are neither essential nor encode enzymes with metabolic flux (Table S4). For 3 of the 11 genes, the fitness defect can be explained by polar effects because an essential or flux-carrying gene is encoded downstream of the target gene and in the same operon. The remaining eight genes may have previously unrecognized functions that have strong effects on cellular fitness.

The average response time of the 253 bottleneck genes was 7.8 h, which is relatively late compared to the seven most sensitive targets that had a response time below 4 h (red dots in Figure 2F). The seven most sensitive targets were: the *ilvE/ilvD* operon, *ppc*, *sucA, lpxC*, *cysD*, *pyrG*, and the *nrdA/nrdB* operon. A hypothesis is that these genes encode enzymes that are rate-limiting steps and therefore they are expressed near-critical levels. For example, ribonucleoside-diphosphate reductase (NrdAB) supplies deoxyribonucleotide triphosphates (dNTPs) for DNA replication, and previous work showed that NrdAB is rate limiting for DNA synthesis (Gon et al., 2006). Similarly, PEP carboxylase (Ppc) supplies tricarboxylic acid (TCA)-cycle precursors for biosynthesis of 10 out of the 20 amino acids (*anaplerosis*). Thus, near-critical Ppc levels may limit overall protein synthesis. This hypothesis is supported by the observation that overexpression of Ppc increases the growth rate of *E. coli* (Chao and Liao, 1993).

In summary, only 7 out of the 1,513 metabolism-related genes had response times below 4 h. The majority of knockdowns, however, responded late to the induction of CRISPRi (on average 7.8 h). This suggests that *E. coli* is robust against reducing the abundance of most metabolic enzymes and that few enzymes are expressed near-critical levels. Next, we wondered how strongly the abundance of target enzymes decreased and which mechanisms buffered the decreases of enzymes.

CRISPRi Enforces Consistent Decreases of Target Enzymes and Specific Proteome Responses

To probe how strongly CRISPRi downregulated the target enzymes, we measured the proteomes of 30 CRISPRi strains (Figure 3A and Table S5). The target enzymes included one of the most sensitive targets in the pooled CRISPRi screen: Ppc that converts PEP to oxaloacetate in *E. coli*. We also included PckA, which catalyzes the reverse reaction and should have no relevance for growth on glucose. Other targets were distributed over the metabolic subsystems, such as glycolysis (Pts, Pgi, PfkA, PfkB, FbaA, GapA, Eno, TpiA, PykA, and PykF) and the oxidative pentose-phosphate pathway (Zwf and Gnd). From the TCA cycle, we selected the first step catalyzed by citrate synthase (GltA), as well as the succinate dehydrogenase complex (SdhABCD). Furthermore, eight target enzymes were in biosynthesis pathways of amino acids (AroA, IlvC, MetE, and GdhA) and nucleotides (Adk, PyrF, PurB, and PurC), or both (Prs and CarAB). The remaining targets were CysH in sulfur assimilation, GlmS in amino sugar biosynthesis, and Dxs in the isoprenoid pathway. We cultured these strains in microtiter plates and measured their proteomes 4.5 h after dCas9 induction. At this time point, growth phenotypes appeared in 10 out of 30 CRISPRi strains (Figures 3B and S5). Each strain was cultured in triplicates with and without induction of dCas9, resulting in a total of 180 proteome samples.

The proteome data showed that all target enzymes decreased to a similar extent (in average 5.1-fold, Figures 3C and S6). In 20 of 29 knockdowns, the target enzyme was the most downregulated protein among all 1,506 measured proteins (Figure S7). Target enzymes hardly decreased in uninduced cultures, showing that the CRISPRi system is tight and inducible (Figure 3C). We confirmed for the PfkA and MetE strain that target enzymes were also downregulated at earlier time points (Figure S8), supporting our assumption that target enzymes decrease progressively after induction of CRISPRi (similar to the YPet knockdown, Figure 1B).

Intuitively, stronger decreases of the target enzyme should cause a stronger growth defect. However, there was no correlation between decreases of target enzymes and reduction of growth (Figure S9). This again indicates that repression efficiencies have smaller effects on growth phenotypes than target-specific factors (e.g., overcapacities of the target enzyme itself). However, we observed a correlation between the reduction of growth and the number of significantly changed proteins (2-fold, p value < 0.05, Figure S9). This means that strains with a growth defect had stronger proteome changes, whereas the proteome was stable in strains without a growth defect. We then analyzed if these proteome changes were a global growth-dependent response (Scott et al., 2010) or if proteome changes were specific. As the average similarity of proteome changes between pairs of CRISPRi strains was only 6% (Figure S10), we concluded that each knockdown caused specific proteome changes. For example, the proteome changes affected different metabolic subsystems (Figure S11), and in some CRISPRi strains (Pts, AroA, MetE, CarAB, and IlvC), enzymes in the same metabolic subsystem as the target enzymes were upregulated (green dots in Figure S7).

In summary, CRISPRi decreased the abundance of target enzymes by an average of 5-fold (Figure 3C). Decreases of target enzymes hardly affected the growth of 19 CRISPRi strains, while growth rates of 10 CRISPRi strains declined ~1 h before the sampling time point (Figure 3B). Thus, *E. coli* metabolism tolerates substantial decreases of enzyme levels and we next wondered which mechanisms enable this robustness.

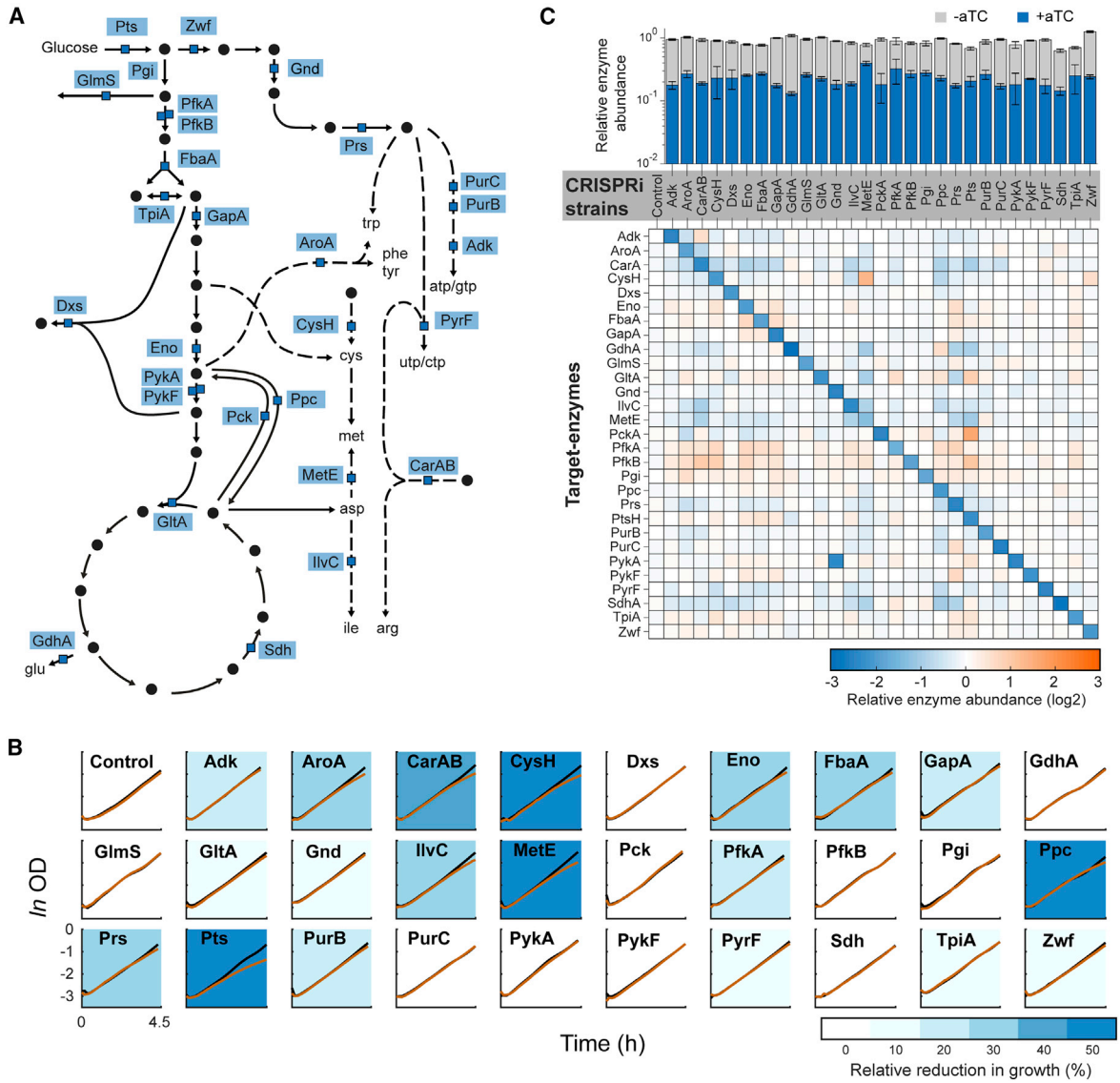

Figure 3. Growth Defects and Abundances of Target Enzymes in 30 CRISPRi Strains

(A) Metabolic map showing the target enzymes of 29 CRISPRi strains. The control strain expressed a sgRNA without a spacer sequence. Operon structures of the targets are shown in Figure S6. See also Table S5.

(B) Growth curves of the 30 CRISPRi strains. See also Table S6. Uninduced cultures are shown in black. Induced cultures are shown in orange (200 nM aTc was supplemented at time = 0 h). Samples for proteomics were collected at the end of the cultivation (4.5 h). Growth curves show means of n = 3 cultures. Background colors indicate the reduction in growth rates at the time of sampling. Growth rates were estimated using linear regression with the last 4 time points of growth curves. Abbreviations of target enzymes are described in Table S5.

(C) The bar plot shows abundances of target enzymes in cultures with inducer (blue) and without inducer (gray). Data are normalized to the average enzyme-level in uninduced cultures. The heatmap shows fold-changes of target enzymes between induced and uninduced cultures. Data were calculated using the means of n = 3 samples per strain, error bars are propagated errors. See also Table S7. See also Figures S5–S11.

Substrates and Allosteric Effectors Respond to CRISPRi-Knockdowns of Enzymes

To understand how *E. coli* metabolism responded to the ~5-fold decrease of target enzymes, we measured the metabolome of the 30 CRISPRi strains. Therefore, we collected samples for metabolomics at the same time point as proteomics samples (4.5 h) and measured 119 intracellular metabolites by liquid chromatography-tandem mass spectrometry (LC-MS/MS). Especially substrate metabolites responded strongly and specifically to knockdowns of enzymes (Figure 4). In 18 out of 29 knockdowns, the substrate increased more than 2-fold and was one of the most changing metabolites. Products, in contrast, were more stable than substrates (Figures 4 and S12). This observation is consistent with a study in yeast, which suggested that increases of substrates can maintain fluxes and global metabolite homeostasis (Fendt et al., 2010).

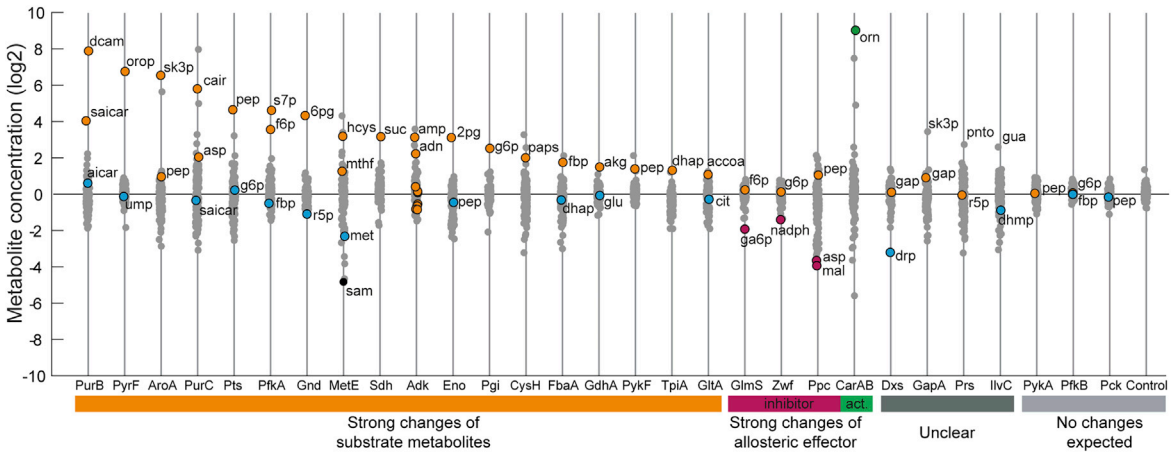

Figure 4. Metabolome Changes in 30 CRISPRi Strains Are Local and Specific

Intracellular concentration of 119 metabolites in the 30 CRISPRi strains. See also Table S8. Metabolite levels are shown as $\log_2$ fold change between induced and uninduced cultures. Samples were collected after 4.5-h cultivation in 12-well plates (see Figure 3B). Data are represented as mean (n = 2). Substrates of the target enzymes are shown in orange, products in blue, allosteric inhibitors in magenta, and allosteric activators are green. SAM in the MetE strain is shown in black (related to Figure 6). Note that isomers were not separated: g6p and f6p is the total pool of hexose-phosphates, r5p is the total pool of pentose- phosphates, dhap and gap are the total pool dhap/gap. Abbreviations of metabolites are described in Table S5. See also Figure S12.

In four strains, allosteric effectors of the target enzyme responded most strongly to the knockdown (CarAB, GlmS, Ppc, and Zwf; Figure 4). Ornithine, for example, is an allosteric activator of carbamoyl phosphate synthetase (CarAB) and ornithine increased 512-fold in the CarAB knockdown. As ornithine levels in *E. coli* are 37-fold lower than the activation constant of CarAB (Bennett et al., 2009; Bueso et al., 1999), increases of ornithine should lead to a 92% higher activity of CarAB *in vivo* (Figure S13). Thus, allosteric activation of CarAB by ornithine could buffer the CarAB knockdown. Similarly, knockdown of Ppc decreased the concentration of aspartate (13-fold) and malate (16-fold), which are both allosteric inhibitors of Ppc. Absolute concentrations of malate and aspartate are above the respective inhibition constants of Ppc (Bennett et al., 2009; Gold and Smith, 1974). Therefore, decreases of aspartate and malate should relieve inhibition of Ppc, which increases its activity 4.1-fold in the Ppc knockdown (Figure S13). In the GlmS and Zwf strain, we observed a similar relieve from allosteric inhibition, because the respective reaction product glucosamine-P and NADPH decreased. This is in line with previous work showing that decreases of NADPH release overcapacities of Zwf (Christodoulou et al., 2018) and that glucosamine-P is a potent inhibitor of GlmS activity (Deng et al., 2006).

In conclusion, knockdowns of enzymes caused specific and localized metabolome changes: 22 CRISPRi strains showed strong concentration changes of either the substrate metabolite or a known allosteric effector of the target enzyme. In four CRISPRi strains (Dxs, GapA, Prs, and IlvC) we could not directly link substrates or known effectors to the target enzyme, although in the Dxs knockdown the product metabolite (1-deoxyxylulose-5-phosphate) decreased strongly and might be an unknown regulator of the enzyme. Three other CRISPRi strains showed no metabolome changes, which was expected because the target enzyme is not used on glucose (Pck) or a minor isoenzyme (PfkB and PykA). The local and specific metabolome changes in the CRISPRi strains are in line with previous work on enzyme-level perturbations (Fendt et al., 2010; Kacser and Burns, 1973), which proposed that local metabolome changes buffer against global changes. Next, we sought to obtain further evidence for a buffering function of metabolite concentration changes in three CRISPRi strains (CarAB, MetE, and Gnd).

Ornithine Buffers the CarAB Knockdown

Despite their potential to buffer knockdowns, allosteric effectors are probably not responding to CRISPRi because they are regulators, but rather because they are located up- or downstream of the target enzyme. For example, ornithine increases in the CarAB knockdown are most likely because ornithine carbamoyltransferase (ArgF and ArgI) is limited due to low levels of the CarAB product carbamoyl phosphate (Figure 5A). This also implies that allosteric activation of CarAB by ornithine cannot fully compensate the CarAB knockdown. Nevertheless, ornithine could have a buffering function that alleviates the consequences of the knockdown. To understand the regulatory role of ornithine in the CarAB knockdown, we developed a small metabolic model of CarAB and the arginine-pyrimidine branch point (STAR Methods and Figure 5A). Kinetic parameters of the model were randomly sampled 1,000 times from physiologically meaningful ranges based on *in vitro* parameters. With each of the 1,000 parameter sets, we simulated the CarAB knockdown using two different models: the first model included allosteric activation of CarAB by ornithine (allosteric model), and the second model did not include this regulation (non-allosteric model). The allosteric model was more robust against the CarAB knockdown than the non-allosteric model (Figure 5B). Especially fluxes remained relatively constant in the allosteric model: 796 of the 1,000 simulations maintained 95% of the initial steady-state flux. In contrast, the flux in the non-allosteric model decreased continuously to about 50% of the initial steady state. Moreover, concentrations of the end products, arginine and UTP/CTP, were

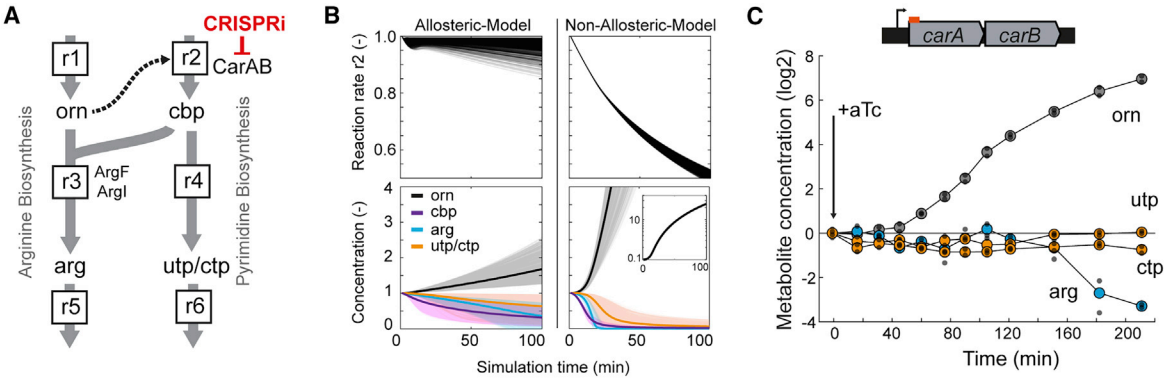

Figure 5. Ornithine Buffers the CarAB Knockdown

(A) Stoichiometry of the kinetic model of CarAB and the arginine-pyrimidine branch point. The dotted arrow indicates allosteric activation of CarAB by ornithine (orn).

(B) Simulation results of the allosteric model and the non-allosteric model with 1,000 parameter sets (thin lines). Thick lines are the average of 1,000 simulations. Shown are the simulated reaction rate of r2 and metabolite dynamics of ornithine (orn, black), carbamoyl phosphate (cbp, purple), arginine (arg, blue) and UTP/CTP (orange). CRISPRi was simulated by setting the expression rate of CarAB to zero at t = 0 min. The insert shows the full range average ornithine levels in the non-allosteric model. (C) Measured concentration of orn, arg, UTP, and CTP in the CarAB knockdown. Metabolite levels are normalized to the time point before induction. The culture was induced with aTc at t = 0 min. Small gray dots are measurements in n = 2 cultures and large colored dots are the mean. See also Figure S13.

more stable in the allosteric model than in the non-allosteric model. These model results suggest that allosteric activation of CarAB by ornithine can minimize perturbations to metabolic flux and end products in arginine and pyrimidine nucleotide biosynthesis.

To confirm the model results, we measured metabolites dynamically in the CarAB knockdown (Figure 5C). Consistent with the simulation results, ornithine had already increased 40 min after induction of the CarAB knockdown, while the end products, arginine, CTP, and UTP remained relatively constant for at least 2 h. The fast response of ornithine shows that the CarAB knockdown perturbs the arginine-pyrimidine branch point early after induction of CRISPRi. However, the perturbation did not propagate into the end products of both pathways. Thus, the combination of a metabolic model and dynamic metabolite data provides additional evidence that ornithine has the potential to buffer the CarAB knockdown.

S-Adenosylmethionine Causes a Compensatory Upregulation of the Methionine Pathway in the MetE Knockdown

Metabolome changes can also modulate gene expression through allosteric interactions between metabolites and transcription factors. For example, S-adenosylmethionine (SAM) is an allosteric activator of MetJ, which is a transcription factor that controls genes involved in methionine and SAM biosynthesis (Figure 6A). SAM was the most decreased metabolite in the MetE knockdown (Figure 4), and, correspondingly, all enzymes in the methionine biosynthesis pathway were upregulated in the MetE strain (except the target MetE, Figure 6B). Thus, we hypothesized that low levels of SAM deactivated the transcription factor MetJ, which in turn de-repressed expression of genes that encode enzymes in methionine and SAM biosynthesis. To confirm that MetJ responded to the MetE knockdown, we expressed GFP in the MetE strain using a MetJ regulated promoter (Zaslaver et al., 2006). Indeed, GFP expression increased with a 2-h delay after induction of CRISPRi, showing that MetJ responded to the knockdown (Figure 6C). Thus, we concluded that low SAM levels caused a compensatory upregulation of the methionine pathway. This hypothesis is supported by SAM levels in all 30 CRISPRi strains: only two strains had low SAM levels (MetE and Ppc strains), and methionine biosynthesis enzymes increased only in those strains (Figure S14).

Next, we wondered if the SAM-MetJ regulation buffered the MetE knockdown. Therefore, we supplemented SAM to the MetE strain and expected that this would prevent decreases of SAM and, consequently, the compensatory upregulation of the methionine pathway. The growth defect of the induced MetE strain was indeed stronger in the presence of SAM (Figure 6D), thus indicating that decreases of SAM buffered the knockdown. The stronger growth defect in the presence of SAM was not due to a general toxic effect, as the uninduced MetE strain was not influenced by SAM (Figure 6D).

In summary, proteome and metabolome data recovered the known allosteric interaction between SAM and the transcription factor MetJ. GFP-promoter fusions confirmed that this regulation is active in the MetE knockdown, and supplementing SAM supported the hypothesis that SAM buffered the MetE knockdown. Similar to the SAM-MetJ interaction, the metabolome/proteome data recovered interactions between arginine and ArgR (active in the CarAB strain), acetyl-serine and CysB (active in the MetE and CysH strains), and transcriptional attenuation by valine (active in the IlvC strain) (Figure S14). This highlights the potential of CRISPRi and multi-omics data to identify regulatory metabolite-protein interactions that are functional *in vivo*.

6-Phosphogluconate Activates the ED Pathway to Bypass the Gnd Knockdown

Knockdown of Gnd increased the concentration of 6-phosphogluconate (6PG) (Figure 4), and upregulated enzymes in the ED

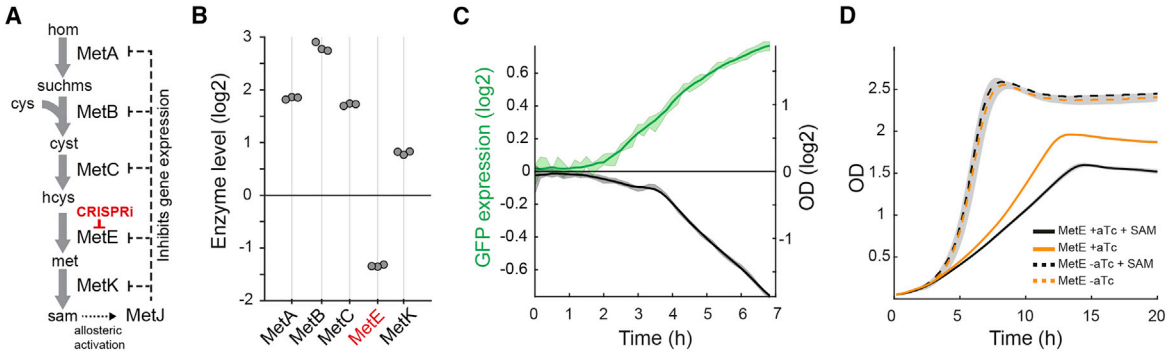

Figure 6. SAM Buffers the MetE Knockdown

(A) Schematic of methionine and SAM biosynthesis and regulation by the transcription factor MetJ.

(B) Abundance of enzymes in methionine and SAM biosynthesis in the MetE strain. See also Table S7. Enzyme levels are shown as $\log_2$ fold change between induced and uninduced cultures (n = 3 cultures).

(C) The MetE knockdown was transformed with a fluorescent reporter plasmid that expressed GFP from a MetJ regulated promoter (pUA66-*metB-gfp*). The fold change of GFP/OD between induced and uninduced cultures is shown in green. The fold change of OD is shown in black.

(D) Growth of the induced MetE strain (full lines) and the uninduced MetE strain (dashed lines), with supplementation of 1 mM SAM (black) and without (orange). Lines in (C) and (D) are means of n = 3 cultures, and shadows show the SD. Induced cultures were supplemented with 200 nM aTc at t = 0 h. See also Figure S14.

pathway (Figures 7A and 7B). Thus, we wondered whether increases in 6PG were linked to the upregulation of the ED pathway. Transcription of the ED pathway is regulated by two transcriptional repressors: KdgR and GntR. While KdgR controls only the two genes encoding the ED enzymes (Edd and Eda), GntR controls additional genes that are involved in gluconate uptake. One enzyme encoded by these genes (GntT) was also upregulated in the Gnd knockdown (Figure 7B), suggesting that GntR responded to the knockdown. The activity of GntR is allosterically inhibited by gluconate (Izu et al., 1997). Therefore, we assumed that the accumulation of 6PG produced small amounts of gluconate, which inhibited GntR and derepressed transcription of *edd* and *eda*. Indeed, the intracellular concentration of gluconate increased in the Gnd knockdown (Figure 7C). The concentration of gluconate was 50 μM in the uninduced Gnd strain, which is close to the wild-type levels (42 μM) (Bennett et al., 2009). Induction of the Gnd knockdown increased gluconate to 184 μM, which was probably sufficient to inhibit GntR and derepress expression of *edd* and *eda*.

Increases of gluconate in the Gnd knockdown suggests that gluconate acts as a regulatory metabolite, which does not participate in metabolism but in regulation. We expected that we could alter this regulation by disrupting the interconversion between 6-phosphogluconate and gluconate. Therefore, we deleted gluconate kinase (*gntK*) in the Gnd knockdown, which led to even higher gluconate levels in the Gnd knockdown (246 μM uninduced, and 620 μM induced, Figure 7C). The higher gluconate levels also increased the expression of the ED enzymes (Figure 7C). The higher abundance of ED enzymes, in turn, reduced 6PG levels in the Δ*gntK*/Gnd knockdown, showing that the ED pathway is a bypass that enables overflow of excess 6PG.

In summary, the Gnd knockdown revealed a bypass function of the ED pathway, which has been observed before in the Gnd knockout (Jiao et al., 2003; McCloskey et al., 2018b). Here, we discovered that expression of the ED-bypass is regulated by 6PG, which is first converted into gluconate and then interacts with the transcription factor GntR.

DISCUSSION

Robustness is a fundamental feature of metabolism. A key requirement for metabolic robustness is that small changes in enzymes levels have no global effects on overall metabolism. Otherwise, fluctuating enzyme levels could decrease metabolic flux and eventually cellular fitness. Theories such as metabolic control analysis predicted that metabolism is insensitive to enzyme-level perturbations (Chandra et al., 2011; Grimbs et al., 2007; Kacser and Burns, 1973; Levine and Hwa, 2007) but have not measured this property at a system level. Studies that measured flux-enzyme-metabolite relationships at a system level examined the impact of nutritional changes on the metabolism of yeast (Hackett et al., 2016) and *E. coli* (Gerosa et al., 2015). However, how changes in enzyme levels affect metabolism is largely unexplored.

In this study, we used CRISPRi to perturb the expression of single enzymes and found that metabolism buffers fitness defects during the initial phase after the induction of CRISPRi. The opposite effect has been reported for CRISPRi-knockdowns in *Bacillus subtilis* (Peters et al., 2016), where a constant knockdown (~3-fold) prolonged initial lag-phases but did not affect growth during exponential phase. Here, we observed that growth defects appeared with a time delay, and only a few strains in a metabolism-wide CRISPRi library responded within the first 3–4 h (*ilvE/ilvD*, *ppc*, *sucA*, *lpxC*, *cysD pyrG*, and *nrdA/nrdB*). Earlier studies support the high sensitivity of these targets, e.g., NrdAB seems rate limiting for DNA synthesis (Gon et al., 2006) and the overexpression of Ppc increases the growth of *E. coli* (Chao and Liao, 1993). The high sensitivity of the *ilvE/ilvD* operon is probably due to the frameshift mutation upstream of *ilvG*, which causes suboptimal expression of these genes (Parekh and Hatfield, 1997). LpxC catalyzes the first committed step in lipid A biosynthesis and the enzyme is a drug target for antimicrobials (Löppenberg et al., 2013). Sensitive targets in glycolysis were mostly located in lower glycolysis, while upper glycolysis enzymes (PfkA and Pgi) had longer response times (Table S4). This

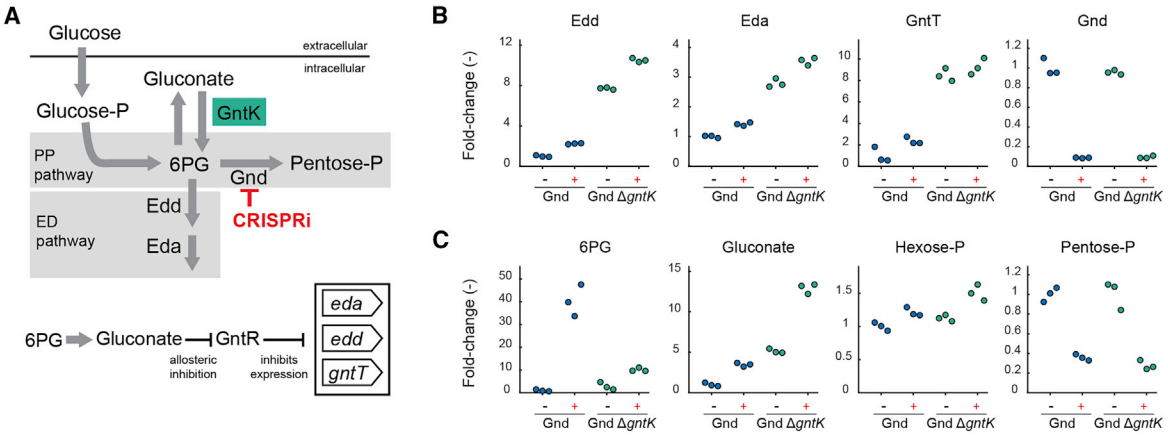

Figure 7. 6-Phosphogluconate Buffers the Gnd Knockdown

(A) Schematic of the ED pathway (two enzymes Edd and Eda), and the oxidative pentose-phosphate pathway. GntK is a kinase that phosphorylates gluconate. Intracellular gluconate can derive from dephosphorylation of 6PG.

(B) Fold-changes of the target enzyme (Gnd), and fold-changes of all measured proteins that are regulated by the transcription factor GntR (Edd, Eda, and GntT). Shown are induced (+) and uninduced (−) knockdowns of Gnd in the YYdCas9 strain (blue) and the YYdCas9-Δ*gntK* strain (green). Samples were collected after 4.5-h cultivation in 12-well plates. Data are normalized to the uninduced Gnd strain (n = 3 cultures).

(C) Same as in (B) for intracellular metabolites. See also Table S9.

observation is in line with previous reports about a thermodynamic bottleneck in lower glycolysis of *E. coli* (Flamholz et al., 2013).

Metabolome and proteome responses of 30 CRISPRi strains were local and specific, and together they indicated that metabolism buffers the decrease of enzymes. This observation is supported by previous reports about overcapacities in metabolism, such as enzyme overabundance (Davidi and Milo, 2017; O'Brien et al., 2016; Sander et al., 2019), reserve fluxes (Christodoulou et al., 2018), or overflow metabolism (Basan et al., 2015; Reaves et al., 2013). It has been suggested that cells control these overcapacities through metabolites that interact with enzymes directly (Christodoulou et al., 2018) or metabolites that modulate gene expression (Sander et al., 2019; Basan et al., 2015). Substrate metabolites, for instance, can modulate enzyme activity through Michaelis-Menten relationships and, thereby, buffer enzyme-level perturbations (Fendt et al., 2010) or modulate metabolic flux (Hackett et al., 2016). The strong increase of substrates in 18 knockdowns indicates that substrate-level regulation could be relevant in these strains. However, it remains open whether these responses buffered lower enzyme levels because *in vivo* kinetic parameters demonstrated that most of the enzymes are saturated (Bennett et al., 2009; Park et al., 2016). Yet, our three case studies (CarAB, MetE, and Gnd) demonstrated that regulatory metabolites can contribute to buffering decreases of enzymes. Future studies could further probe the buffering capacity of metabolites by repressing the target gene at a lesser (or stronger) extent (Hawkins et al., 2020), and measure whether this leads to milder (or stronger) metabolome and proteome changes.

In conclusion, our study shows that the metabolome responds specifically and locally to enzyme-level perturbations by CRISPRi and that *E. coli* tolerates substantial decreases of enzymes. This supports the prevailing hypothesis that the abundance of single enzymes has little effects on metabolic flux and that local changes in metabolism do not propagate globally (Kacser and Burns, 1973). This mechanism may ensure a high constancy of metabolic flux despite expression noise (Newman et al., 2006; Taniguchi et al., 2010) or mutations that occur during the evolution of metabolic networks (McCloskey et al., 2018a).

STAR★METHODS

Detailed methods are provided in the online version of this paper and include the following:

- KEY RESOURCES TABLE
- RESOURCE AVAILABILITY
  - Lead Contact
  - Materials Availability
  - Data and Code Availability
- EXPERIMENTAL MODEL AND SUBJECT DETAILS
  - Strains and Culture
  - Construction of Arrayed Strains
  - Construction of the CRISPRi Pooled Library
  - Media
- METHOD DETAILS
  - Cultivation Conditions for OD and YPet-, GFP-Fluorescence Measurements
- CULTIVATION CONDITIONS FOR METABOLOME AND PROTEOME SAMPLING
  - Cultivation Conditions of the Pooled CRISPRi Library
  - Next Generation Sequencing and Data Analysis
  - Constraint-Based Modeling
  - Kinetic Modelling of the CarAB Knockdown
  - Metabolomics Measurements
  - Proteomics Sample Preparation and Measurement
- QUANTIFICATION AND STATISTICAL ANALYSIS

SUPPLEMENTAL INFORMATION

Supplemental Information can be found online at https://doi.org/10.1016/j.cels.2020.10.011.

ACKNOWLEDGMENTS

We thank T.J. Erb, V. Sourjik, and A. Diepold for discussions. We thank J. Elf for providing the YYdCas9 strain. This work has received funding from the European Research Council (ERC) under the European Union's Horizon 2020 research and innovation program (grant agreement no. 715650, ERC Starting Grant MapMe). S.D. and M.K. acknowledge funding from the IMPRS graduate school for environmental, cellular, and molecular microbiology from the Max Planck Society. L.R. acknowledges funding from DFG SPP2141.

AUTHOR CONTRIBUTIONS

S.D. performed experiments with arrayed CRISPRi strains, analyzed data, performed FBA analysis, and co-wrote the manuscript. M.K. performed experiments with the pooled CRISPRi library and co-wrote the manuscript. M.K. and S.D. analyzed data from the pooled CRISPRi screen. V.P. performed experiments with arrayed CRISPRi strains. N.F. developed and analyzed the CarAB model. D.B. constructed the pooled CRISPRi library. M.K., J.V.G.F., and L.R. performed Illumina sequencing. T.G. measured proteomes. C.-Y.W. performed experiments. H.L. conceived the study, analyzed data, and co-wrote the manuscript.

DECLARATION OF INTERESTS

The authors declare no competing interests.

Received: March 16, 2020
Revised: September 23, 2020
Accepted: October 29, 2020
Published: November 24, 2020

REFERENCES

Baba, T., Ara, T., Hasegawa, M., Takai, Y., Okumura, Y., Baba, M., Datsenko, K.A., Tomita, M., Wanner, B.L., and Mori, H. (2006). Construction of *Escherichia coli* K-12 in-frame, single-gene knockout mutants: the Keio collection. Mol. Syst. Biol. *2*, 2006.0008.

Basan, M., Hui, S., Okano, H., Zhang, Z., Shen, Y., Williamson, J.R., and Hwa, T. (2015). Overflow metabolism in *E. coli* results from efficient proteome allocation. Nature *528*, 99–104.

Bennett, B.D., Kimball, E.H., Gao, M., Osterhout, R., Van Dien, S.J., and Rabinowitz, J.D. (2009). Absolute metabolite concentrations and implied enzyme active site occupancy in *Escherichia coli*. Nat. Chem. Biol. *5*, 593–599.

Buescher, J.M., Liebermeister, W., Jules, M., Uhr, M., Muntel, J., Botella, E., Hessling, B., Kleijn, R.J., Le Chat, L., Lecointe, F., et al. (2012). Global network reorganization during dynamic adaptations of *Bacillus subtilis* metabolism. Science *335*, 1099–1103.

Bueso, J., Cervera, J., Fresquet, V., Marina, A., Lusty, C.J., and Rubio, V. (1999). Photoaffinity labeling with the activator IMP and site-directed mutagenesis of histidine 995 of carbamoyl phosphate synthetase from *Escherichia coli* demonstrate that the Binding Site for IMP overlaps with that for the inhibitor UMP. Biochemistry *38*, 3910–3917.

Camsund, D., Lawson, M.J., Larsson, J., Jones, D., Zikrin, S., Fange, D., and Elf, J. (2020). Time-resolved imaging-based CRISPRi screening. Nat. Methods *17*, 86–92.

Chandra, F.A., Buzi, G., and Doyle, J.C. (2011). Glycolytic oscillations and limits on robust efficiency. Science *333*, 187–192.

Chao, Y.P., and Liao, J.C. (1993). Alteration of growth yield by overexpression of phosphoenolpyruvate carboxylase and phosphoenolpyruvate carboxykinase in *Escherichia coli*. Appl. Environ. Microbiol. *59*, 4261–4265.

Christodoulou, D., Link, H., Fuhrer, T., Kochanowski, K., Gerosa, L., and Sauer, U. (2018). Reserve flux capacity in the pentose phosphate pathway enables *Escherichia coli*'s rapid response to oxidative stress. Cell Syst. *6*, 569–578.e7.

Davidi, D., and Milo, R. (2017). Lessons on enzyme kinetics from quantitative proteomics. Curr Opin Biotechnol *46*, 81–89.

Dekel, E., and Alon, U. (2005). Optimality and evolutionary tuning of the expression level of a protein. Nature *436*, 588–592.

Deng, M.D., Grund, A.D., Wassink, S.L., Peng, S.S., Nielsen, K.L., Huckins, B.D., and Burlingame, R.P. (2006). Directed evolution and characterization of *Escherichia coli* glucosamine synthase. Biochimie *88*, 419–429.

Ebrahim, A., Lerman, J.A., Palsson, B.O., and Hyduke, D.R. (2013). COBRApy: COnstraints-based reconstruction and analysis for Python. BMC Syst. Biol. *7*, 74.

Erickson, D.W., Schink, S.J., Patsalo, V., Williamson, J.R., Gerland, U., and Hwa, T. (2017). A global resource allocation strategy governs growth transition kinetics of *Escherichia coli*. Nature *551*, 119–123.

Fendt, S.M., Buescher, J.M., Rudroff, F., Picotti, P., Zamboni, N., and Sauer, U. (2010). Tradeoff between enzyme and metabolite efficiency maintains metabolic homeostasis upon perturbations in enzyme capacity. Mol. Syst. Biol. *6*, 356.

Flamholz, A., Noor, E., Bar-Even, A., Liebermeister, W., and Milo, R. (2013). Glycolytic strategy as a tradeoff between energy yield and protein cost. Proc. Natl. Acad. Sci. USA *110*, 10039–10044.

Fuhrer, T., Zampieri, M., Sévin, D.C., Sauer, U., and Zamboni, N. (2017). Genomewide landscape of gene–metabolome associations in *Escherichia coli*. Mol. Syst. Biol. *13*, 907.

Gerosa, L., Haverkorn van Rijsewijk, B.R.B., Christodoulou, D., Kochanowski, K., Schmidt, T.S.B., Noor, E., and Sauer, U. (2015). Pseudo-transition analysis identifies the key regulators of dynamic metabolic adaptations from steady-state data. Cell Syst. *1*, 270–282.

Gerosa, L., Kochanowski, K., Heinemann, M., and Sauer, U. (2013). Dissecting specific and global transcriptional regulation of bacterial gene expression. Mol. Syst. Biol. *9*, 658.

Giaever, G., Chu, A.M., Ni, L., Connelly, C., Riles, L., Véronneau, S., Dow, S., Lucau-Danila, A., Anderson, K., André, B., et al. (2002). Functional profiling of the *Saccharomyces cerevisiae* genome. Nature *418*, 387–391.

Gold, E.W., and Smith, T.E. (1974). *Escherichia coli* phosphoenolpyruvate carboxylase: effect of allosteric inhibitors on the kinetic parameters and sedimentation behavior. Arch. Biochem. Biophys. *164*, 447–455.

Gon, S., Camara, J.E., Klungsøyr, H.K., Crooke, E., Skarstad, K., and Beckwith, J. (2006). A novel regulatory mechanism couples deoxyribonucleotide synthesis and DNA replication in *Escherichia coli*. EMBO J. *25*, 1137–1147.

Grimbs, S., Selbig, J., Bulik, S., Holzhütter, H.G., and Steuer, R. (2007). The stability and robustness of metabolic states: identifying stabilizing sites in metabolic networks. Mol. Syst. Biol. *3*, 146.

Guder, J.C., Schramm, T., Sander, T., and Link, H. (2017). Time-optimized isotope ratio LC–MS/MS for high-throughput quantification of primary metabolites. Anal. Chem. *89*, 1624–1631.

Hackett, S.R., Zanotelli, V.R.T., Xu, W., Goya, J., Park, J.O., Perlman, D.H., Gibney, P.A., Botstein, D., Storey, J.D., and Rabinowitz, J.D. (2016). Systems-level analysis of mechanisms regulating yeast metabolic flux. Science *354*, aaf2786.

Hawkins, J.S., Silvis, M.R., Koo, B.M., Peters, J.M., Osadnik, H., Jost, M., Hearne, C.C., Weissman, J.S., Todor, H., and Gross, C.A. (2020). Mismatch-CRISPRi reveals the co-varying expression-fitness relationships of essential genes in Escherichia coli and Bacillus subtilis. Cell Syst. *11*, 1–13.

Hosseini, S.R., and Wagner, A. (2018). Genomic organization underlying deletional robustness in bacterial metabolic systems. Proc. Natl. Acad. Sci. USA *115*, 7075–7080.

Ishii, N., Nakahigashi, K., Baba, T., Robert, M., Soga, T., Kanai, A., Hirasawa, T., Naba, M., Hirai, K., Hoque, A., et al. (2007). Multiple high-throughput analyses monitor the response of *E. coli* to perturbations. Science *316*, 593–597.

Izu, H., Adachi, O., and Yamada, M. (1997). Gene organization and transcriptional regulation of the gntRKU operon involved in gluconate uptake and catabolism of *Escherichia coli*. J. Mol. Biol. *267*, 778–793.

Jensen, K.F. (1993). The *Escherichia coli* K-12 "wild types" W3110 and MG1655 have an rph frameshift mutation that leads to pyrimidine starvation due to low *pyrE* expression levels. J. Bacteriol. *175*, 3401–3407.

Jiao, Z., Baba, T., Mori, H., and Shimizu, K. (2003). Analysis of metabolic and physiological responses to *gnd* knockout in *Escherichia coli* by using C-13 tracer experiment and enzyme activity measurement. FEMS Microbiol. Lett. *220*, 295–301.

Jones, D.L., Leroy, P., Unoson, C., Fange, D., Ćurić, V., Lawson, M.J., and Elf, J. (2017). Kinetics of dCas9 target search in *Escherichia coli*. Science *357*, 1420–1424.

Kacser, H., and Burns, J.A. (1973). The control of flux. Symp. Soc. Exp. Biol. *27*, 65–104.

Kacser, H., and Burns, J.A. (1981). The molecular basis of dominance. Genetics *97*, 639–666.

Kemmeren, P., Sameith, K., van de Pasch, L.A.L., Benschop, J.J., Lenstra, T.L., Margaritis, T., O'Duibhir, E., Apweiler, E., van Wageningen, S., Ko, C.W., et al. (2014). Large-scale genetic perturbations reveal regulatory networks and an abundance of gene-specific repressors. Cell *157*, 740–752.

Keren, L., Hausser, J., Lotan-Pompan, M., Vainberg Slutskin, I., Alisar, H., Kaminski, S., Weinberger, A., Alon, U., Milo, R., and Segal, E. (2016). Massively parallel interrogation of the effects of gene expression levels on fitness. Cell *166*, 1282–1294.e18.

Keren, L., Zackay, O., Lotan-Pompan, M., Barenholz, U., Dekel, E., Sasson, V., Aidelberg, G., Bren, A., Zeevi, D., Weinberger, A., et al. (2013). Promoters maintain their relative activity levels under different growth conditions. Mol. Syst. Biol. *9*, 701.

King, Z.A., Lu, J., Dräger, A., Miller, P., Federowicz, S., Lerman, J.A., Ebrahim, A., Palsson, B.O., and Lewis, N.E. (2016). BiGG Models: a platform for integrating, standardizing and sharing genome-scale models. Nucleic Acids Res. *44*, D515–D522.

Lawson, M.J., Camsund, D., Larsson, J., Baltekin, Ö., Fange, D., and Elf, J. (2017). *In situ* genotyping of a pooled strain library after characterizing complex phenotypes. Mol. Syst. Biol. *13*, 947.

Levine, E., and Hwa, T. (2007). Stochastic fluctuations in metabolic pathways. Proc. Natl. Acad. Sci. USA *104*, 9224–9229.

Li, G.W., Burkhardt, D., Gross, C., and Weissman, J.S. (2014). Quantifying absolute protein synthesis rates reveals principles underlying allocation of cellular resources. Cell *157*, 624–635.

Löppenberg, M., Müller, H., Pulina, C., Oddo, A., Teese, M., Jose, J., and Holl, R. (2013). Synthesis and biological evaluation of flexible and conformationally constrained LpxC inhibitors. Org. Biomol. Chem. *11*, 6056–6070.

Mazat, J.P., Reder, C., and Letellier, T. (1996). Why are most flux control coefficients so small? J. Theor. Biol. *182*, 253–258.

McCloskey, D., Xu, S., Sandberg, T.E., Brunk, E., Hefner, Y., Szubin, R., Feist, A.M., and Palsson, B.O. (2018a). Evolution of gene knockout strains of *E. coli* reveal regulatory architectures governed by metabolism. Nat. Commun. *9*, 3796.

McCloskey, D., Xu, S., Sandberg, T.E., Brunk, E., Hefner, Y., Szubin, R., Feist, A.M., and Palsson, B.O. (2018b). Growth adaptation of gnd and sdhCB *Escherichia coli* deletion strains diverges from a similar initial perturbation of the transcriptome. Front. Microbiol. *9*, 1793.

Metzger, B.P.H., Yuan, D.C., Gruber, J.D., Duveau, F., and Wittkopp, P.J. (2015). Selection on noise constrains variation in a eukaryotic promoter. Nature *521*, 344–347.

Monk, J.M., Lloyd, C.J., Brunk, E., Mih, N., Sastry, A., King, Z., Takeuchi, R., Nomura, W., Zhang, Z., Mori, H., et al. (2017). iML1515, a KnowledgeBase that computes *Escherichia coli* traits. Nat. Biotechnol. *35*, 904–908.

Mülleder, M., Calvani, E., Alam, M.T., Wang, R.K., Eckerstorfer, F., Zelezniak, A., and Ralser, M. (2016). Functional metabolomics describes the Yeast biosynthetic regulome. Cell *167*, 553–565.e12.

Newman, J.R.S., Ghaemmaghami, S., Ihmels, J., Breslow, D.K., Noble, M., DeRisi, J.L., and Weissman, J.S. (2006). Single-cell proteomic analysis of *S. cerevisiae* reveals the architecture of biological noise. Nature *441*, 840–846.

O'Brien, E.J., Utrilla, J., and Palsson, B.O. (2016). Quantification and Classification of E. coli Proteome Utilization and Unused Protein Costs across Environments. PLoS Comput Biol *12*, e1004998.

Parekh, B.S., and Hatfield, G.W. (1997). Growth rate-related regulation of the ilvGMEDA operon of *Escherichia coli* K-12 is a consequence of the polar frameshift mutation in the ilvG gene of this strain. J. Bacteriol. *179*, 2086–2088.

Park, J.O., Rubin, S.A., Xu, Y.F., Amador-Noguez, D., Fan, J., Shlomi, T., and Rabinowitz, J.D. (2016). Metabolite concentrations, fluxes and free energies imply efficient enzyme usage. Nat. Chem. Biol. *12*, 482–489.

Peters, J.M., Colavin, A., Shi, H., Czarny, T.L., Larson, M.H., Wong, S., Hawkins, J.S., Lu, C.H.S., Koo, B.M., Marta, E., et al. (2016). A comprehensive, CRISPR-based functional analysis of essential genes in Bacteria. Cell *165*, 1493–1506.

Qi, L.S., Larson, M.H., Gilbert, L.A., Doudna, J.A., Weissman, J.S., Arkin, A.P., and Lim, W.A. (2013). Repurposing CRISPR as an RNA-guided platform for sequence-specific control of gene expression. Cell *152*, 1173–1183.

Reaves, M.L., Young, B.D., Hosios, A.M., Xu, Y.F., and Rabinowitz, J.D. (2013). Pyrimidine homeostasis is accomplished by directed overflow metabolism. Nature *500*, 237–241.

Rishi, H.S., Toro, E., Liu, H., Wang, X., Qi, L.S., and Arkin, A.P. (2020). Systematic genome-wide querying of coding and non-coding functional elements in *E. coli* using CRISPRi. Biorxiv. https://doi.org/10.1101/2020.03.04.975888.

Rousset, F., Cui, L., Siouve, E., Becavin, C., Depardieu, F., and Bikard, D. (2018). Genome-wide CRISPR-dCas9 screens in E. coli identify essential genes and phage host factors. PLoS Genet. *14*, e1007749.

Sander, T., Farke, N., Diehl, C., Kuntz, M., Glatter, T., and Link, H. (2019). Allosteric feedback inhibition enables robust amino acid biosynthesis in *E. coli* by enforcing enzyme overabundance. Cell Syst. *8*, 66–75.e8.

Schmidt, A., Kochanowski, K., Vedelaar, S., Ahrné, E., Volkmer, B., Callipo, L., Knoops, K., Bauer, M., Aebersold, R., and Heinemann, M. (2016). The quantitative and condition-dependent *Escherichia coli* proteome. Nat. Biotechnol. *34*, 104–110.

Scott, M., Gunderson, C.W., Mateescu, E.M., Zhang, Z., and Hwa, T. (2010). Interdependence of cell growth and gene expression: origins and consequences. Science *330*, 1099–1102.

Taniguchi, Y., Choi, P.J., Li, G.W., Chen, H., Babu, M., Hearn, J., Emili, A., and Xie, X.S. (2010). Quantifying *E. coli* proteome and transcriptome with single-molecule sensitivity in single cells. Science *329*, 533–538.

Tanner, L.B., Goglia, A.G., Wei, M.H., Sehgal, T., Parsons, L.R., Park, J.O., White, E., Toettcher, J.E., and Rabinowitz, J.D. (2018). Four key steps control glycolytic flux in mammalian cells. Cell Syst *7*, 49–62.e8.

Towbin, B.D., Korem, Y., Bren, A., Doron, S., Sorek, R., and Alon, U. (2017). Optimality and sub-optimality in a bacterial growth law. Nat. Commun. *8*, 14123.

Tran, L.M., Rizk, M.L., and Liao, J.C. (2008). Ensemble modeling of metabolic networks. Biophys. J. *95*, 5606–5617.

You, C., Okano, H., Hui, S., Zhang, Z., Kim, M., Gunderson, C.W., Wang, Y.P., Lenz, P., Yan, D., and Hwa, T. (2013). Coordination of bacterial proteome with metabolism by cyclic AMP signalling. Nature *500*, 301–306.

Zaslaver, A., Bren, A., Ronen, M., Itzkovitz, S., Kikoin, I., Shavit, S., Liebermeister, W., Surette, M.G., and Alon, U. (2006). A comprehensive library of fluorescent transcriptional reporters for *Escherichia coli*. Nat. Methods *3*, 623–628.

Zelezniak, A., Vowinckel, J., Capuano, F., Messner, C.B., Demichev, V., Polowsky, N., Mülleder, M., Kamrad, S., Klaus, B., Keller, M.A., et al. (2018). Machine learning predicts the yeast metabolome from the quantitative proteome of kinase knockouts. Cell Syst. *7*, 269–283.e6.

STAR★METHODS

KEY RESOURCES TABLE

REAGENT or RESOURCE	SOURCE	IDENTIFIER
Bacterial and Virus Strains		
NEB 5-alpha Competent E. coli: fhuA2 Δ(argF-lacZ)U169 phoA glnV44 Φ80 Δ(lacZ) M15 gyrA96 recA1 relA1 endA1 thi-1 hsdR17	New England Biolabs	Cat#C2987
YYdCas9: BW25993 intC::tetR-dcas9-aadA lacY::ypet-cat	Lawson et al., 2017	N/A
YYdCas9: BW25993 CRISPRi-pgRNA_cntrl: intC::tetR-dcas9-aadA lacY::ypet-cat	This study	N/A
YYdCas9: BW25993 CRISPRi-pgRNA_carAB: intC::tetR-dcas9-aadA lacY::ypet-cat pUA66-PargE-gfp	This study	N/A
YYdCas9: BW25993 CRISPRi-pgRNA_metE: intC::tetR-dcas9-aadA lacY::ypet-cat pUA66-PmetB-gfp	This study	N/A
BW25113: F-, Δ(araD-araB)567, ΔlacZ4787(::rrnB-3), λ-, ΔgntK768::kan, rph-1, Δ(rhaD-rhaB)568, hsdR514	Baba et al., 2006	JW3400-1
Genotypes and spacer sequences of arrayed CRISPRi strains are listed in Table S11	N/A	N/A
Genotypes and spacer sequences of pooled CRISPRi strains are listed in Table S1	N/A	N/A
Chemicals, Peptides, and Recombinant Proteins		
Acetonitrile	Honeywell Riedel-de Haën	Cat#14261-2L
Methanol	VWR	Cat#83638.320
Anhydrotetracycline	Sigma-Aldrich	Cat#1035708-25MG
IPTG	Roth	Cat#CN08.2
Ampicillin	Roth	Cat#K029.2
Kanamycin	Roth	Cat#T832.3
Critical Commercial Assays		
PierceTM Quantitative Colometric Peptide Assay	Thermo Fisher Scientific	Cat#23275
PierceTM BCA Protein Assay Kit	Thermo Fisher Scientific	Cat#23225
Deposited Data		
Kinetic Model	github.com/nfarke/Donati_Kuntz_et_al	N/A
NGS Data	http://www.ebi.ac.uk/ena/data/view/PRJEB40851	PRJEB40851
Metabolomics data	https://edmond.mpdl.mpg.de/imeji/collection/u_8nsTTnbzAExmuZ	N/A
Proteomics data	https://www.ebi.ac.uk/pride/archive/projects/PXD022070	PXD022070
Oligonucleotides		
Oligonucleotides are listed in Table S10	Eurofins	N/A
Recombinant DNA		
pgRNA-bacteria	Qi et al., 2013	Addgene plasmid #44251

(*Continued on next page*)

Continued

REAGENT or RESOURCE	SOURCE	IDENTIFIER
pUA66-PargE-gfp: pPargE-gfp	Zaslaver et al., 2006	N/A
pUA66-PmetB-gfp: pPmetB-gfp	Zaslaver et al., 2006	N/A
Software and Algorithms		
Matlab R2018b (9.5.0.944444) for analysis of experimental data	mathworks.com	N/A
Python 3.7.4	python.org	N/A
COBRApy	opencobra.github.io/cobrapy	N/A
Progenesis QIP (Waters)	waters.com	N/A
MASCOT (v2.5, Matrix Science)	matrixscience.com	N/A
SafeQuant	https://cran.r-project.org/web/packages/SafeQuant/index.html	N/A

RESOURCE AVAILABILITY

Lead Contact

Further information and requests for resources and reagents should be directed to and will be fulfilled by the Lead Contact, Hannes Link (hannes.link@synmikro.mpi-marburg.mpg.de).

Materials Availability

Plasmids and strains generated in this study are available on request from the Lead Contact, Hannes Link (hannes.link@synmikro.mpi-marburg.mpg.de).

Data and Code Availability

Sequencing source data have been deposited at the European Nucleotide Archive (ENA) and are publicly available under the accession number: PRJEB40851. Proteome source data have been deposited at the PRIDE database and are publicly available under the accession numbers: PXD022070. Metabolome source data have been deposited at the Open Research Data Repository of the Max Planck Society (Edmond) and are publicly available at: https://edmond.mpdl.mpg.de/imeji/collection/u_8nsTTnbzAExmuZ . Original code of the CarAB model is publicly available at the GitHub repository: https://github.com/nfarke/Donati_Kuntz_et_al. Scripts used to generate the figures presented in this paper are not provided in this paper but are available from the Lead Contact on request. Any additional information required to reproduce this work is available from the Lead Contact.

EXPERIMENTAL MODEL AND SUBJECT DETAILS

Strains and Culture

E. coli YYdCas9 strain (Lawson et al., 2017) was the wild-type strain used in this study. NEB 5-alpha Competent *E. coli* (Cat#C2987) cells were used for cloning. All strains in this study derive from the YYdCas9 strain and are listed in the Key Resources Table.

Construction of Arrayed Strains

30 CRISPRi strains were created by transforming the YYdCas9 (Lawson et al., 2017) strain with pgRNA-bacteria plasmids that harbor the respective sgRNA (Addgene #44251). The spacer of sgRNAs consisted of a gene specific 20–22 base-pair region, which pairs adjacent to an NGG PAM site. The spacers were designed to bind as close as possible to the start of the coding sequence (Table S11). Addgene #44251 was used as a template to prepare all plasmids, which were cloned inhouse or provided by Doulix. All plasmids were validated by sequencing. For CRISPRi of YPet, the sgRNA targeted *lacZ*, the first gene of the operon that includes YPet (Lawson et al., 2017). The plasmid pUA66 was used to measure promoter activity (Zaslaver et al., 2006). The Δ*gntK* mutant was constructed by P1 Phage transduction of YYdCas9 using the donor strain JW3400 (Δ*gntK*) from the KEIO collection (Baba et al., 2006). The resulting strain was cured from the kanamycin resistance gene included in the transduction cassette. The deletion of *gntK* was confirmed by sequencing. The final YYdCas9_Δ*gntK* strain was transformed with the pgRNA-*gnd* plasmid.

Construction of the CRISPRi Pooled Library

sgRNA guide sequences were designed with MATLAB scripts by searching for 4 to 6 equally distributed NGG PAM sites on the coding strand of each gene in the iML1515 model (Monk et al., 2017). Adjacent to PAM sites, 20 nt regions were selected. 150 nt oligonucleotides were synthesized (Agilent Technologies, USA). The 150 nt sequences contained the 20 nt sgRNA guide sequences and 65 nt flanking regions homologous to the pgRNA-bacteria backbone. Oligonucleotides were amplified with 15 cycles of PCR amplification. The pgRNA-bacteria backbone (containing the nontargeting spacer sequence 5'-AACTTTCAGTTTAGCGGTCT-3') was

linearized by PCR and amplified oligonucleotides were inserted with Gibson assembly. The Gibson assembly product was purified and subsequently transformed into electrocompetent *E. coli* YYdCas9 cells. Plating on four Petri dishes with 15 cm diameter resulted in approximately 9.9 × 10^7 colonies. Colonies were washed from the plates, pooled and stored as glycerol stocks.

Media

Cultivations were performed with LB medium or M9 minimal medium with glucose as sole carbon source (5 g L^{-1}). M9 medium was composed by (per liter): 7.52 g Na_2HPO_4 2 H_2O, 5 g KH_2PO_4, 1.5 g $(NH_4)2_SO_4$, 0.5 g NaCl. The following components were sterilized separately and then added (per liter of final medium): 1 mL 0.1 M $CaCl_2$, 1 mL 1 M $MgSO_4$, 0.6 mL 0.1 M $FeCl_3$, 2 mL 1.4 mM thiamine-HCl and 10 mL trace salts solution. The trace salts solution contained (per liter): 180 mg $ZnSO_4$ 7 H2O, 120 mg $CuCl_2$ 2 H_2O, 120 mg $MnSO_4$ H2O, 180 mg $CoCl_2$ 6 H_2O. For strains transformed with pgRNA-bacteria plasmids, 100 μg mL^{-1} ampicillin (Amp) was added to the media. To induce expression of the dCas9 protein in the YYdCas9 strain, aTc was added to a final concentration of 200 nM. In experiments with pUA66 plasmids 34 μg mL^{-1} kanamycin was added to the medium.

METHOD DETAILS

Cultivation Conditions for OD and YPet-, GFP-Fluorescence Measurements

Single colonies on LB+Amp agar plates were transferred into 5 mL LB+Amp liquid cultures. The LB pre-cultures were used to inoculate a second pre-culture in M9 medium that was incubated overnight in 13 mL culture tubes under shaking at 37°C. M9 pre-cultures were diluted in 150 μL M9 medium (1:50) and incubated in 96-well plates. Every strain was cultured in triplicates with and without addition of aTc to the M9 main culture (aTc was not added to pre-cultures). For YPet fluorescence measurements, 0.1 mM IPTG was added to pre-cultures and main cultures to induce YPet expression. Optical density (600 nm) and YPet fluorescence (excitation 510 nm, emission 540 nm) was measured every 5 min using a plate reader (BioTek, Synergy). For GFP measurements, GFP fluorescence (excitation 490 nm, emission 530 nm) was measured in 10 min intervals using a plate reader (Tecan, Grödig, Austria, Spark).

CULTIVATION CONDITIONS FOR METABOLOME AND PROTEOME SAMPLING

Single colonies were transferred into liquid 5 mL LB+Amp from fresh LB+Amp plates, and then re-inoculated in M9 medium overnight in 13 mL culture tubes under shaking at 37 °C. For metabolomics and proteomics sampling, M9 pre-cultures were adjusted to a starting OD_{600} of 0.05 into 12-well plates, with 2 mL of medium in each well. Strains were cultivated in triplicates with or without aTc, added at the beginning of the culture. Optical density at 600nm was measured every 10 min using a plate reader (Tecan, Spark) for 4.5 h. Plates were then rapidly transferred to a thermostatically controlled hood at 37 °C and kept shaking during the sampling procedure. For dynamic metabolomics, M9 pre-cultures were adjusted to a starting OD_{600} of 0.05 in a beaker containing 50 mL of medium and a magnetic stirrer. Beakers were incubated with 400 rpm magnetic stirring in a thermostatically controlled hood at 37 °C.

Cultivation Conditions of the Pooled CRISPRi Library

A preculture of 50 mL LB+Amp was inoculated with 500 μL of the pooled CRISPRi strain library from a glycerol stock and incubated at 37 °C for 5 hours. From the LB culture a second preculture in M9 was inoculated with a dilution of 1:10000 and incubated for 13 hours. After 13 hours the M9 preculture was in exponential phase and it was used to inoculate two main cultures with an initial OD of 0.05 in shaking flasks containing 100 mL of M9 with 200 nM of aTc to induce expression of dCas9. Every hour, OD was measured and samples for sequencing were collected. Every 2 hours, the culture was back-diluted to an OD of 0.05 with fresh and prewarmed M9 containing 200 nM of aTc. Samples were centrifuged to precipitate the cells and plasmids were extracted with the GeneJET Plasmid MiniPrep Kit (Thermo Fisher Scientific).

Next Generation Sequencing and Data Analysis

To generate the DNA fragments of target regions, which are compatible with Illumina sequencing, a two-step PCR approach was used. First, a 300 bp fragment including the sgRNA sequence and the flanking regions has been amplified using Q5 polymerase (New England Biolabs, USA) and specific oligonucleotides binding at the target region (NGS_F2_adapter and NGS_R2_adapter, Table S10). As template, 150 ng of the purified samples were used in a 50 μL PCR reaction with the following settings: 98 °C for 30 s, 12 cycles of 98 °C for 10 s, 65 °C for 30 s and 72 °C for 15 s; final extension at 72 °C for 5 min. Afterward, the PCR products were purified with a NucleoSpin Gel and PCR Clean-up Kit (Macherey-Nagel, Germany) and eluted in 20 μL water. In the second PCR, when different pairs of indexes (i5 and i7) were added to each amplicon, Phusion High- Fidelity DNA Polymerase (New England BioLabs, USA) was used with the following conditions: 98 °C for 30 s; 12 cycles of 98 °C for 10 s, 55 °C for 30 s and 72 °C for 20 s; final extension at 72 °C for 5 min. 4 ng of template was used in a final volume of 20 μL. Cleanup of the PCR products was done with AMPure XP beads (Beckman Coulter). All samples were run on a Bioanalyzer with an Agilent High Sensitivity DNA Kit (Agilent, USA) to analyze their composition. Next, 100 ng of each sample was pooled and the concentration of the pooled samples was measured using the Qubit dsDNA HS Assay on a Qubit 2.0 Fluorometer. The pooled samples were diluted, denatured and loaded on a MiniSeq High Output Cartridge following the manufacturer's instructions. To guarantee sufficient sequence diversity, 50% PhiX was spiked into the samples. Single-end reads provided sequences, which were mapped to the sgRNAs in the CRISPRi library using a MATLAB Script. Read counts were calculated with single-end sequencing reads that matched to sgRNA guide sequences in the CRISPRi

reference library (Table S1). Read counts per sgRNA ($reads_i$) were normalized to the total number of read counts per sample ($reads_{total}$) to obtain frequencies of sgRNAs. Frequencies were normalized to the first time point (t = 0 h) to calculate fold-changes.

Constraint-Based Modeling

Genes that encode enzymes with metabolic flux during growth on glucose were determined with Flux Balance Analysis (FBA). The *E. coli* *i*ML1515 metabolic model was downloaded from BiGG Models http://bigg.ucsd.edu/ (King et al., 2016) and FBA simulations were applied using COBRApy (Ebrahim et al., 2013) with parameters as described in Monk et al. (2017).

Kinetic Modelling of the CarAB Knockdown

The stoichiometry of the model is shown in Figure 5A. Mass balancing yields a system of ordinary differential equations (ODEs), F, that is a temporal function of the state variables x and the kinetic parameters p:

$$F(x,p) = \frac{dx}{dt} = \begin{cases} \frac{dorn}{dt} = r_1 - r_3 \\ \frac{dcbp}{dt} = r_2 - r_3 - r_4 \\ \frac{darg}{dt} = r_3 - \alpha_1 \cdot \mu_1 \\ \frac{dutp}{dt} = r_4 - \alpha_2 \cdot \mu_2 \\ \frac{de_2}{dt} = -\mu \cdot e_2 \end{cases} \quad \text{(Equation 1)}$$

The six reactions (r_1, r_2, r_3, r_4, μ_1, μ_2) are described by the following kinetic equations:
The influx into the arginine pathway r1 is constant:

$$r_1 = k_{cat1} \quad \text{(Equation 2)}$$

Allosteric activation of reaction r_2 by ornithine follows a power-law function:

$$r_2 = k_{cat,2} \cdot e_2 \cdot \left(\frac{orn}{orn_{SS}}\right)^{K_2} \quad \text{(Equation 3)}$$

where orn_{SS} is the steady state ornithine concentration.
Reaction r_3 follows a non-ordered Bi-uni mechanism:

$$r_3 = k_{cat,3} \cdot \frac{1}{\left(1 + \frac{K_{m_{orn}} \cdot K_{m_{cbp}}}{orn \cdot cbp} + \frac{K_{m_{orn}}}{orn} + \frac{K_{m_{cbp}}}{cbp}\right)} \quad \text{(Equation 4)}$$

Reaction r4 follows simple Michaelis-Menten kinetics:

$$r_4 = k_{cat,4} \cdot \frac{cbp}{cbp + K_4} \quad \text{(Equation 5)}$$

The growth rate μ depends on μ_1 and μ_2, which follow Michaelis-Menten kinetics:

$$r_5 = \mu_{max,1} \cdot \frac{arg}{arg + K_{\mu 1}} \quad \text{(Equation 6)}$$

$$r_6 = \mu_{max,2} \cdot \frac{utp}{utp + K_{\mu 2}} \quad \text{(Equation 7)}$$

$$\mu = mean(\mu_1, \mu_2) \quad \text{(Equation 8)}$$

In total, the model includes 14 kinetic parameters k_{cat1}, k_{cat2}, k_{cat3}, k_{cat4}, K_2, $K_{m,orn}$, $K_{m,cbp}$, K_4, $K_\mu 1$, $K_\mu 2$, μ_{max1}, μ_{max2}, α_1 and α_2. The ensemble modelling approach (Tran et al., 2008) was used to account for uncertainties in kinetic parameters.

First, a steady flux distribution was calculated that is common for all subsequent parameter sets (r_1 = 0.958 mM min^{-1}, r_2 = 1.425 mM min^{-1}, r_3 = 0.958 mM min^{-1}, r_4 = 0.467 mM min^{-1}, μ_1 = 0.958 mM min^{-1}, μ_2 = 0.467 mM min^{-1}). The flux distribution was estimated using flux balance analysis. Arginine and UTP efflux (μ_1 and μ_2) were calculated as the product of their biomass coefficients (α_1 = 95.8 mM, α_2 = 46.7 mM) and the growth rate on glucose (μ = 0.01 min^{-1}).

Binding constants (K-values) and metabolite concentrations (Ornithine = 0.01 mM, UMP = 0.50 mM, Arginine = 0.138 mM) were obtained from literature and Cbp concentration was set to 1 mM. The concentration of e2 was set to 1 mM. The binding constants were sampled 1000 times from 10-fold intervals based on literature values ($K_{m,orn}$ = 0.32 mM (argF/I, Ecocyc), $K_{m,cbp}$ = 0.36 mM (argF/I, Ecocyc), K_4 = 0.028 mM (Brenda ID: 696699), $K_\mu 2$ = 0.05 mM (pyrH, Ecocyc)). The power-law term K_2 was sampled between 1 and 4 in the regulated model and was set to zero in the dysregulated model. $K_\mu 1$ was fixed to 1×10^{-5} mM.

With the ensemble modelling approach the system is initially set into a steady state. To test stability of the steady states, eigenvalues of the Jacobian matrix were calculated, and tested if all eigenvalues are negative ($\lambda < -10^{-6}$). The procedure was repeated until 1000 stable steady states were achieved. The perturbation by CRISPRi was then simulated for all stable models by setting the expression rate of e2 to zero:

$$\frac{de2}{dt} = 0 - \mu \cdot e2 \qquad \text{(Equation 9)}$$

Metabolomics Measurements

Cultivations were performed as described above. Culture aliquots were vacuum-filtered on a 0.45 μm pore size filter (HVLP02500, Merck Millipore). Filters were immediately transferred into a 40:40:20 (v-%) acetonitrile/methanol/water extraction solution at -20 °C. Filters were incubated in the extraction solution for at least 30 minutes. Subsequently, metabolite extracts were centrifuged for 15 minutes at 13,000 rpm at -9 °C and the supernatant was stored at -80 °C until analysis. Metabolite extracts were mixed with a ^{13}C-labeled internal standard in a 1:1 ratio. LC-MS/MS analysis was performed with an Agilent 6495 triple quadrupole mass spectrometer (Agilent Technologies) as described previously (Guder et al., 2017). An Agilent 1290 Infinity II UHPLC system (Agilent Technologies) was used for liquid chromatography. Temperature of the column oven was 30°C, and the injection volume was 3 μL. LC solvents in channel A were either water with 10 mM ammonium formate and 0.1% formic acid (v/v) (for acidic conditions), or water with 10 mM ammonium carbonate and 0.2% ammonium hydroxide (for basic conditions). LC solvents in channel B were either acetonitrile with 0.1% formic acid (v/v) (for acidic conditions) or acetonitrile without additive (for basic conditions). LC columns were an Acquity BEH Amide (30 x 2.1 mm, 1.7 μm) for acidic conditions, and an iHILIC-Fusion(P) (50 x 2.1 mm, 5 μm) for basic conditions. The gradient for basic and acidic conditions was: 0 min 90% B; 1.3 min 40 % B; 1.5 min 40 % B; 1.7 min 90 % B; 2 min 90 % B. The ratio of ^{12}C and ^{13}C peak heights was used to quantify metabolites. ^{12}C/^{13}C ratios were normalized to OD at the time point of sampling. Absolute concentrations of gluconate were determined from ^{12}C peak heights and an external calibration with an authentic standard. A specific cell volume of 2 μL mg^{-1} was used to calculate the cell volume.

Proteomics Sample Preparation and Measurement

Cultivations were performed as described above. Culture aliquots were transferred into 2 mL reaction tubes and washed two times with PBS buffer (0.14 mM NaCl, 2.7 mM KCl, 1.5 KH_2PO_4, 8.1 Na_2HPO_4). Cell pellets were resuspended in 300 μL lysis buffer containing 100 mM ammonium bicarbonate, 0.5 % sodium lauroyl sarcosinate (SLS). Cells were lysed by 5 minutes incubation at 95 °C and ultra-sonication for 10 seconds (Vial Tweeter, Hielscher). Cells were again incubated for 15 minutes with 5 mM Tris(2-carboxyethyl)phosphine (TCEP) at 90°C followed by alkylation with 10 mM iodoacetamide for 15 minutes at 25 °C. To clear the cell lysate, samples were centrifuged for 10 minutes at 15,000 rpm and the supernatant was transferred into a new tube. Protein samples were quantified using a BCA Protein Assay kit (Thermo Fisher Scientific). For each sample, 50 μg of proteins was aliquoted to new tubes, volumes were adjusted and cell lysates were digested with 1 μg trypsin (Promega) overnight at 30°C. SLS was removed by precipitation. Therefore, trifluoroacetic acid (TFA) was added to a final concentration of 1.5 % and incubated at room temperature for 10 minutes. After centrifugation (10 minutes at 10,000 rpm), the supernatant was used for C18 purification of peptides using Micro Spin-Columns (Harvard Apparatus). The purified peptide solutions were dried and resuspended in 0.1 % TFA. The concentration of peptides in the samples was measured with a colorimetric peptide assay (Pierce™ Quantitative Colorimetric Peptide Assay, Thermo Fischer Scientific). Analysis of peptides was performed by with a Q-Exactive Plus mass spectrometer coupled to an Ultimate 3000 RSLC nano with a Prowflow upgrade and a nanospray flex ion source (Thermo Scientific). Peptide separation was performed on a reverse-phase HPLC column (75 μm x 42 cm) packed in-house with C18 resin (2.4 μm, Dr. Maisch GmbH, Germany). The following separating gradient was used: 96 % solvent A (0.15% formic acid) and 4 % solvent B (99,85 % acetonitrile, 0.15 % formic acid) to 30 % solvent B over 60 minutes at a flow rate of 300 nL/min. The data acquisition mode was set to obtain one high resolution MS scan at a resolution of 70,000 full width at half maximum (at m/z 200) followed by MS/MS scans of the 10 most intense ions. To increase the efficiency of MS/MS attempts, the charged state screening modus was enabled to exclude unassigned and singly charged ions. The dynamic exclusion duration was set to 30 seconds. The ion accumulation time was set to 50 ms for MS and 50 ms at 17,500 resolution for MS/MS. The automatic gain control was set to 3x106 for MS survey scans and 1x105 for MS/MS scans. Label-free quantification (LFQ) of the data was performed using Progenesis QIP (Waters), and for MS/MS searches of aligned peptide features MASCOT (v2.5, Matrix Science) was used. The following search parameters were used: full tryptic search with two missed cleavage sites, 10ppm MS1 and 0.02 Da fragment ion tolerance. Carbamidomethylation (C) as fixed, oxidation (M) and deamidation (N,Q) as variable modification. Progenesis outputs were further processed with SafeQuant. The data was further processed with custom MATLAB scripts.

QUANTIFICATION AND STATISTICAL ANALYSIS

Statistical analysis was performed using custom MATLAB scripts. The number of replicates (n) of each experiment can be found in the respective figure caption. In growth assays, n represents the number of independent microtiter plate cultures. For proteomics and metabolomics n represents the number of independent microtiter plate or shake flask cultures. Three replicates were used for metabolomics, and one of the three replicates was removed based on its Euclidean distance from the other two replicates. The remaining two replicates were used to calculate means. This removed outliers in the metabolome data set, which can occur due to the high sensitivity of the metabolome during sampling. In the proteomics dataset, proteins with an average variability between triplicates higher than 20% were removed. This left 1507 proteins that were measured in every sample. Significant proteins were defined with a two-fold cut-off and a p-value<0.05 for a two-sample t-test. Similarity of proteomes was obtained calculating the Jaccard index of significantly differentially expressed proteins.